

DEPARTMENT OF PHYSICS
UNIVERSITY OF JYVÄSKYLÄ
RESEARCH REPORT No. 1/2016

**CHARACTERIZATION OF THREE-DIMENSIONAL
MICROSTRUCTURE OF COMPOSITE MATERIALS BY
X-RAY TOMOGRAPHY**

**BY
ARTTU MIETTINEN**

Academic Dissertation
for the Degree of
Doctor of Philosophy

*To be presented, by the permission of the
Faculty of Mathematics and Science
of the University of Jyväskylä,
for public examination in Auditorium FYS-1 of the
University of Jyväskylä on 15 January 2016
at 12 o'clock*



Jyväskylä, Finland
January, 2016

Abstract

Analysis methods for X-ray microtomographic images of short fibre composite materials were developed. The methods enable estimation of microstructural properties of the material, *e.g.*, aspect ratio and orientation of fibres. Being based on X-ray microtomography and image analysis, the methods are non-destructive and do not require user intervention.

In particular, a method for determination of the aspect ratio of fibres was first developed. The method contains an assumption about similarity of the shape of the fibres. The assumption was relaxed in an improved method that can estimate cross-sectional properties of fibres, too, *e.g.*, cross-sectional area. Additionally, the effect of finite image volume on the results of the measurements was discussed. It was concluded that fibre length is the quantity that is most biased by it. A method for correcting the bias was proposed.

The developed algorithms were tested and applied in estimation of parameters for a micromechanical model and in quantification of morphological degradation of wood fibres in injection moulding process.

It was demonstrated that the methods can be used to measure the parameters of a specific micromechanical model for Young's modulus of flax fibre composites. The modelling results were compared to those calculated with parameters determined manually, and to results of tensile tests.

Morphological degradation of wood fibres in injection moulding process was studied. It was observed that both the length and the aspect ratio of the fibres decrease considerably during processing.

Finally, a special sample holder was fabricated for studying the hygroexpansion of fibres in a wood fibre composite material. Tomographic images acquired with the sample holder were used to estimate expansion parameters of the fibres. The parameters were applied in validating a finite element model.

In all cases discussed above, results obtained using the developed methods are in agreement with those from independent reference measurements.

JYFL Research Report 1/2016
ISBN 978-951-39-6324-8 (paper copy)
ISBN 978-951-39-6325-5 (pdf)
ISSN 0075-465X

Author Arttu Miettinen
Department of Physics
University of Jyväskylä
Finland
Email: arttu.miettinen@phys.jyu.fi

Supervisor Professor Markku Kataja
Department of Physics
University of Jyväskylä
Finland

Reviewers Professor Gunilla Borgefors
Center for Image Analysis
Uppsala University
Sweden

Professor Stepan Lomov
Department of Metallurgy and Materials Engineering
Katholieke Universiteit Leuven
Belgium

Opponent Assistant professor Sabine Rolland du Roscoat
Laboratoire 3SR
l'Université Joseph Fourier
Grenoble
France

List of publications

This thesis is mainly based on the following publications:

1. Miettinen, A., Ojala, A., Wikström, L., Joffe, R., Madsen, B., Nätti-
nen, K. and Kataja, M.: *Non-destructive automatic determination of
aspect ratio and cross-sectional properties of fibres*, Composites: Part A
77:188–194, 2015.
2. Miettinen, A., Luengo Hendriks, C. L., Chinga-Carrasco, G., Gamstedt,
E. K. and Kataja, M.: *A non-destructive X-ray microtomography ap-
proach for measuring fibre length in short-fibre composites*, Composites
Science and Technology 72(15):1901–1908, 2012.
3. Joffe, T., Miettinen, A., Berthold, F. and Gamstedt, E. K.: *X-ray
micro-computed tomography investigation of fibre length degradation
during the processing steps of short-fibre composites*, Composites Science
and Technology 105:127–133, 2014.
4. Joffe, T., Wernersson, E., Miettinen, A., Luengo Hendriks, C. L. and
Gamstedt, E. K.: *Swelling of cellulose fibres in composite materials:
Constraint effects of the surrounding matrix*, Composites Science and
Technology 74:52-59, 2013.

Author's contribution

The author performed the main parts of the X-ray microtomographic experiments for papers 1, 3, and 4 and participated in the experiments made for paper 2. The central parts of the image analysis software was implemented and the main parts of image-based measurements was performed by the author for papers 1, 2, and 3. Initial drafts of papers 1 and 2 were written by the author, who also participated in writing papers 3 and 4.

In addition to the publications above, references [5–10] contain material strongly related to the contents of this thesis.

Contents

Abstract	i
List of publications	v
1 Introduction	1
2 X-ray microtomography	5
2.1 Principles of X-ray microtomography	5
2.2 Reconstruction and image preprocessing	7
2.2.1 Attenuation of X-rays	7
2.2.2 Reconstruction	8
2.2.3 Image preprocessing	12
3 Characterization of the 3D microstructure of composite materials by image analysis	19
3.1 Composite materials	19
3.2 General structural properties	23
3.3 Properties of dispersed particle phase	29
3.4 Properties of interconnected particle phase	34
3.4.1 Fibre length	34
3.4.2 Multivariate size distributions	41
3.5 Finite size corrections	45
4 Applications	49
4.1 Micromechanical modelling	49

4.2	Morphological degradation of fibres in injection moulding process	51
4.3	Swelling of fibres	55
5	Summary	59
	Bibliography	61

Chapter 1

Introduction

Composite materials consist of distinguishable domains of two or more constituents. They often contain a fibrous reinforcing phase and a binder phase that is referred to as matrix. Composite materials occur both naturally and in man-made form. For example, glass fibre composite materials are often used in applications such as boats, gas cylinders and wind turbine blades. Car tyres are made from a composite material comprising reinforcing fibres in rubber matrix. A common example of natural composite material is wood, consisting of cellulose fibres in lignin and hemicellulose matrix. Lately, concern has grown on environmental impact and availability of non-biodegradable materials like glass or carbon fibres. Natural fibres, *e.g.*, flax, hemp or wood, have been suggested as an environmentally friendlier alternative [11].

The shape of the fibres, their orientation, their distribution in the matrix and properties of contacts between matrix and fibres affect the mechanical properties and processability of the composite material. Information about the geometry of the material and factors affecting it could thus be used in, *e.g.*, designing tailored composite materials with specific properties.

Often the size of the fibres and the size of the matrix domains between the fibres are in the range $1\ \mu\text{m} - 1000\ \mu\text{m}$. The structure of the material at that size scale is referred here as the microstructure. Within the traditional

sectioning method for characterization of microstructure, the sample is cut into thin slices, each one containing a part of the internal structure of the material [12–16]. The slices are imaged using suitable two-dimensional imaging modality, *e.g.*, light microscopy or scanning electron microscopy (SEM). When stacked together, the images of the individual slices form a three-dimensional volume image of the sample. If the sample cannot be cut into thin slices as such, it may be embedded into supporting material and the slicing process substituted by grinding or polishing [17].

The sectioning process destroys the sample and thus rules out studying the same sample again, *e.g.*, in varying environmental conditions. Additionally, the sectioning and polishing processes apply large forces to the sample, making those techniques most suitable for rigid materials, such as many glass fibre composites. Natural fibres are often soft and fragile and thus potentially deform in the sectioning process. Hence, it may be difficult to produce clean sections of natural fibre composites.

X-ray tomography is a nondestructive imaging method, where the three-dimensional structure of the sample is computationally reconstructed from two-dimensional X-ray projection images. The structure of the sample can then be quantified by applying image analysis algorithms to the reconstructed three-dimensional image. Lately, various algorithms have been developed for determination of, *e.g.*, volume fractions of constituents, various correlation functions [18], diameters of material domains [19, 20] or orientation of their surfaces [21] from three-dimensional volume images. Such algorithms often form the basis for more advanced and specialized analysis methods, including those that are discussed in this work.

Recently, algorithms that deal with segmentation of individual fibres have been proposed [22–35]. Although such algorithms provide detailed information about the structure of the material and the relations of the individual fibres, they often contain assumptions about the shape of the fibres or about the way the fibres are packed together. The irregular shape of natural fibres may not conform to the assumptions made, and thus such segmentation al-

gorithms may be difficult to apply to tomographic images of natural fibre composites.

In this thesis methods are developed for determination of fibre length, diameter, orientation, and related quantities. Only methods that do not require segmentation of individual fibres from each other are considered. Focus is on methods whose results can be validated with independent measurements. The algorithms discussed in this thesis form a toolbox for analysis of three-dimensional tomographic images of short-fibre composite materials. Some methods discussed in this thesis may be used to analyse also other types of materials, *e.g.*, textile composites and heterogeneous materials in general.

The rest of this thesis is organized as follows. In Section 2 the basics of X-ray tomography are reviewed, including the basic design of a microtomographic scanner, the filtered backprojection reconstruction algorithm and preprocessing of the three-dimensional images. In Section 3 algorithms for determination of the geometrical properties of composite materials are discussed, including methods for determination of multivariate distributions of geometrical properties of fibres. The effects of finite volume of the tomographic image are also covered. Examples of applications of the methods are discussed in Section 4. The focus is on quantification of materials that contain natural fibres as the reinforcing phase. Finally, Section 5 concludes the thesis with a summary.

Chapter 2

X-ray microtomography

2.1 Principles of X-ray microtomography

X-ray microtomography (X- μ CT) [36–45] is based on taking a large number of two-dimensional X-ray projection images of the sample from various directions. The three-dimensional structure of the sample is reconstructed computationally from the two-dimensional projections. Notable advantages of the method are that the sample is not destroyed in the imaging process and that only very little sample preparation is typically needed. It is normally enough to cut the sample into a shape that approximately fits into the field-of-view of the tomographic scanner.

A typical microtomographic device (Figure 2.1) contains an X-ray source that produces radiation directed towards the sample. The sample, mounted on a rotation stage, attenuates the radiation before it hits a scintillating plate that converts X-rays into visible light. The light is imaged by a digital camera mounted on a microscope that provides additional magnification.

In X- μ CT imaging process, the sample is placed into the device and the first X-ray projection image is recorded. The rotation stage rotates the sample slightly and the next X-ray projection image is recorded. The process repeats until the sample has rotated at least 180° . Finally, a computer reconstructs

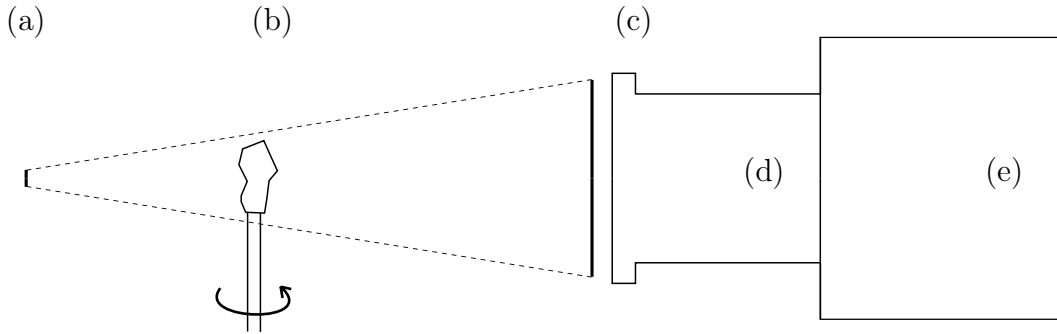


Figure 2.1: Schematic illustration of a cone beam X- μ CT scanner. (a) X-ray source, (b) sample mounted on a rotating sample holder, (c) scintillating plate, (d) microscope objective and (e) camera. The dashed lines represent a cone of X-rays.

the three-dimensional structure from the projections. The contrast in the three-dimensional image may originate from X-ray absorption in the region-of-interest or from the phase shift of the X-rays, the former being the most commonly used imaging modality in tabletop-scale devices.

The type of the X-ray source classifies X- μ CT devices into two categories based on imaging geometry: cone beam and parallel beam. Cone beam devices are typically based on a microfocus X-ray tube, where an electron beam is accelerated and focused into a small spot on a metal target. The X-rays, formed by the decelerating electrons, emanate from the spot to all directions. Part of the radiation exits the tube through a window, forming a cone-shaped beam. The shape of the beam can be utilized to tune the magnification by simply changing the position of the sample relative to the X-ray source: as the sample is moved towards the X-ray source, the size of its projection on the scintillating plate increases, thereby increasing magnification.

Parallel beam X- μ CT devices are typically based on a synchrotron light source [46]. In a synchrotron, electrons are accelerated to relativistic energies. The electron beam is routed through insertion devices (undulators, wigglers) that force it to move on a curved path thus producing radiation. Due to relativistic effects, the observed frequency of the emitted radiation is in the

X-ray regime, and the beam contracts into a very sharp cone. As the angular divergence of the X-rays is close to zero, the source is said to produce parallel beam radiation. The properties of the insertion device and monochromators control the spectrum of X-rays. The intensity of the X-ray beam is very high, allowing an order-of-magnitude faster X- μ CT scans than a system based on a microfocus X-ray tube.

The resolving power of an X- μ CT device is fundamentally limited by the resolution of the scintillating plate, the microscope-camera system used to record the projection images, the quality of the X-ray beam and the mechanical stability of the system. However, in cone-beam devices, the limiting factor is often the size of the spot where the X-rays are emitted from. For a hypothetical singular source, there would be only a single ray path between any point in the scintillating plate and the source. For a real finite source, there are multiple such ray paths for each point at the scintillating plate. Thus, each point in the plate receives X-ray attenuation information from multiple paths through the sample, smearing out small details. Typically, source spot sizes in microfocus tubes are near $5\ \mu\text{m}$ [47, 48] and the corresponding image resolutions near $2.5\ \mu\text{m}$.

2.2 Reconstruction and image preprocessing

2.2.1 Attenuation of X-rays

X-rays entering the sample may pass directly through or interact with the material in various ways. In the X-ray energy range often applied in X-ray microtomography ($\lesssim 100\ \text{kV}$), the most relevant phenomena are Photoelectric effect and Compton scattering [49]. For the purpose of this thesis, one can ignore the details of the interactions and study only the effective attenuation of X-rays in the sample. Denote one ray path through the sample by C , x being the position on the path. Denoting X-ray intensity by I , the change in

I on a small piece of the path is

$$dI = -\mu_{\text{eff}}(x)I(x)dx, \quad (2.1)$$

where μ_{eff} is the effective linear attenuation coefficient. Integration gives

$$-\ln \frac{I}{I_0} = \int_C \mu_{\text{eff}}(x)dx, \quad (2.2)$$

where I_0 is the X-ray intensity before entering the sample. Equation (2.2) is also known as the Beer-Lambert law. It should be noted that this equation is strictly true only for monochromatic X-rays, but in practice the artefacts resulting from its application to polychromatic radiation can be relatively well corrected for [49].

The I/I_0 term on the left side of Equation (2.2) is measured by the X- μ CT scanner on a large number of straight ray paths from the X-ray source to the scintillating plate. The reconstruction process then estimates the values of μ_{eff} based on the measured data, thus producing a three-dimensional volumetric image of the sample.

2.2.2 Reconstruction

There are various algorithms for reconstructing the spatial distribution of μ_{eff} , which constitutes the X- μ CT image [50]. Here, only the filtered back-projection algorithm for parallel beam geometry will be briefly discussed [38, 40, 41]. For a cone beam geometry, the algorithm is essentially the same, but substantially different weighting of the projection images must be applied [44, 45].

It is first assumed that the X-ray beam is parallel and the directions of the ray paths from the X-ray source to the camera are normal to the rotation axis. Consider a single plane perpendicular to the rotation axis. By the assumption above, all the ray paths that intersect the selected plane are confined into it.

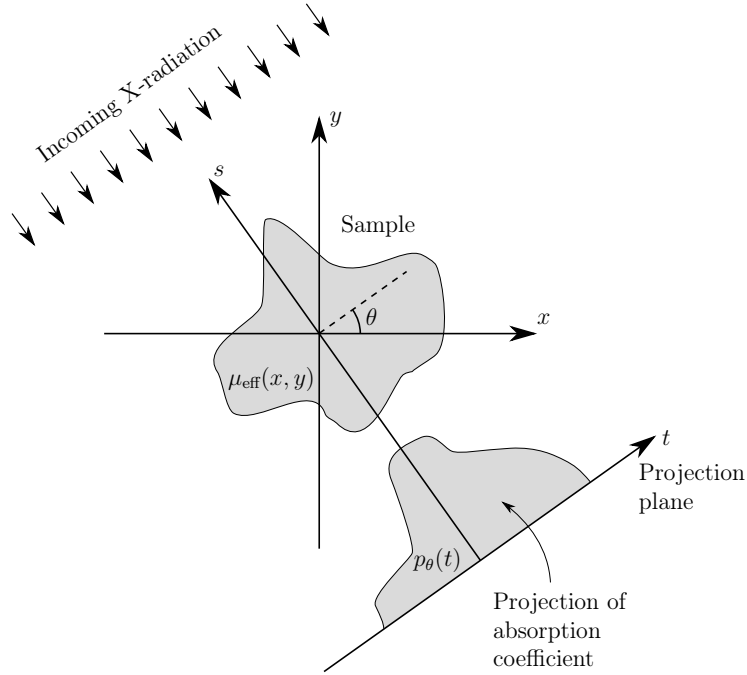


Figure 2.2: Coordinate systems in the filtered backprojection algorithm. (t, s) -coordinates are rotated by θ with respect to (x, y) -coordinates.

All the planes perpendicular to the rotation axis are thus independent from each other and it is sufficient to consider only one of them at a time.

Denote by (x, y) coordinates on the selected plane, origin being placed on the rotation axis. Furthermore, denote by (t, s) coordinates rotated by θ around the origin (Figure 2.2),

$$\begin{aligned} t &= x \cos \theta + y \sin \theta \\ s &= -x \sin \theta + y \cos \theta. \end{aligned} \tag{2.3}$$

In the (t, s) -coordinates, the s -axis is parallel to the direction of the ray paths. The projection of μ_{eff} to the t -axis is

$$p_\theta(t) = \int_{-\infty}^{\infty} \mu_{\text{eff}}(t, s) ds, \tag{2.4}$$

whose Fourier transform is given by

$$\tilde{p}_\theta(\omega) = \int_{-\infty}^{\infty} p_\theta(t) e^{-2\pi i \omega t} dt. \quad (2.5)$$

Substituting Equation (2.4) into Equation (2.5), and noting that the Jacobian determinant of the coordinate transformation in Equation (2.3) is unity, gives

$$\tilde{p}_\theta(\omega) = \int_{-\infty}^{\infty} \int_{-\infty}^{\infty} \mu_{\text{eff}}(x, y) e^{-2\pi i \omega (x \cos \theta + y \sin \theta)} dx dy. \quad (2.6)$$

On the other hand, the two-dimensional Fourier transform of μ_{eff} is given by

$$\tilde{\mu}_{\text{eff}}(u, v) = \int_{-\infty}^{\infty} \int_{-\infty}^{\infty} \mu_{\text{eff}}(x, y) e^{-2\pi i (xu + yv)} dx dy. \quad (2.7)$$

Comparing Equation (2.6) and Equation (2.7) gives

$$\tilde{p}_\theta(\omega) = \tilde{\mu}_{\text{eff}}(\omega \cos \theta, \omega \sin \theta) \equiv M(\omega, \theta). \quad (2.8)$$

This result is known as the Fourier slice theorem or the Projection slice theorem. Equation (2.8) suggests a way to reconstruct μ_{eff} from the projections p_θ . According to Equation (2.8) the values of the one-dimensional Fourier transforms of the projections could be used to approximate specific values in the two-dimensional Fourier transform of the image. Inverse Fourier transform would then yield the image μ_{eff} . In practice such a reconstruction requires sophisticated interpolation schemes as the Fourier transforms of the projections do not sample the two-dimensional Fourier space evenly. However, it is possible to continue from the Fourier slice theorem to arrive in an algorithm that does not require such interpolation.

Write the inverse Fourier transform of $\tilde{\mu}_{\text{eff}}(u, v)$ as

$$\mu_{\text{eff}}(x, y) = \int_{-\infty}^{\infty} \int_{-\infty}^{\infty} \tilde{\mu}_{\text{eff}}(u, v) e^{2\pi i (xu + yv)} du dv \quad (2.9)$$

and change to polar coordinates using the transformation

$$u = \omega \cos \theta \quad (2.10)$$

$$v = \omega \sin \theta. \quad (2.11)$$

The Jacobian determinant for this transformation is ω , so that

$$\mu_{\text{eff}}(x, y) = \int_{\theta=0}^{2\pi} \int_{\omega=0}^{\infty} M(\omega, \theta) e^{2\pi i \omega (x \cos \theta + y \sin \theta)} \omega d\omega d\theta. \quad (2.12)$$

Using $M(\omega, \theta + \pi) = M(-\omega, \theta)$ and dividing the θ -integration into $0 \rightarrow \pi$ and $\pi \rightarrow 2\pi$ gives

$$\mu_{\text{eff}}(x, y) = \int_{\theta=0}^{\pi} \int_{\omega=-\infty}^{\infty} M(\omega, \theta) e^{2\pi i \omega (x \cos \theta + y \sin \theta)} |\omega| d\omega d\theta. \quad (2.13)$$

Substituting Fourier slice theorem Equation (2.8) into Equation (2.13) gives

$$\mu_{\text{eff}}(x, y) = \int_{\theta=0}^{\pi} \int_{\omega=-\infty}^{\infty} \tilde{p}_{\theta}(\omega) e^{2\pi i \omega (x \cos \theta + y \sin \theta)} |\omega| d\omega d\theta \quad (2.14)$$

$$= \int_0^{\pi} p'_{\theta}(x \cos \theta + y \sin \theta) d\theta, \quad (2.15)$$

where

$$p'_{\theta}(t) = \int_{-\infty}^{\infty} \tilde{p}_{\theta}(\omega) |\omega| e^{2\pi i \omega t} d\omega. \quad (2.16)$$

This result is known as the filtered backprojection algorithm. First, Equation (2.16) indicates that prior to further processing, the projection data must be filtered with a filter whose frequency response is $|\omega|$. Equation (2.15) describes the backprojection phase. It means that $\mu_{\text{eff}}(x, y)$ can be written as a sum of relevant values of the filtered projections p'_{θ} . The relevant values are those that would contain a contribution of $\mu_{\text{eff}}(x, y)$ if the projection was calculated. On the other hand, a value of a filtered projection contributes equally to μ_{eff} at all (x, y) for which it is relevant. Thus, the backprojection process can be understood as smearing the projections onto the image and summing over all the smears, see Figure 2.3.

Figure 2.3(a) shows a computer-generated test structure, whose projections $p_\theta(t)$ are shown in Figure 2.3(b). The projections filtered according to Equation (2.16) are shown in Figure 2.3(c). Reconstructions obtained with 2, 8 and 180 filtered projections are shown in Figures 2.3(d), (e) and (f), respectively. It is easy to see how the reconstructed μ_{eff} approaches the original as the count of projections increases.

2.2.3 Image preprocessing

In many practical cases, the images obtained using X- μ CT contain spurious noise and artefacts that must be attenuated before further processing. Additionally, for some image processing algorithms presented in the following sections, the different material phases must be partitioned from each other into separate images. These processes, referred to as filtering and segmentation, respectively, are discussed in detail in many textbooks and other treatments like Gonzalez and Woods [51] and Turpeinen [52]. Thus, only the most basic methods will be reviewed in this section.

Let us begin by modelling a typical image degradation process by

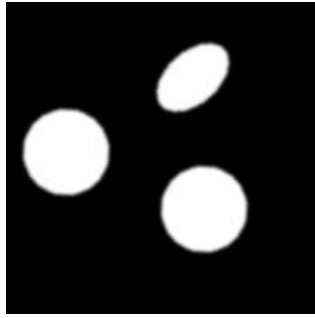
$$\mu_{\text{eff}} = h * \mu'_{\text{eff}} + n, \quad (2.17)$$

where μ_{eff} is the degraded image, μ'_{eff} is the undegraded image, h is a degradation function, n is random noise and $*$ denotes convolution (see *e.g.* [51]). The purpose of filtering is to estimate μ'_{eff} based on the measured data μ_{eff} . The functions h and n are unknown, and additionally, n typically varies from image to image, although its statistical properties may remain constant.

In the context of this thesis, attenuating the noise term n is the most crucial part. Let us thus assume that h is identity and simplify the Equation (2.17) to

$$\mu_{\text{eff}} = \mu'_{\text{eff}} + n. \quad (2.18)$$

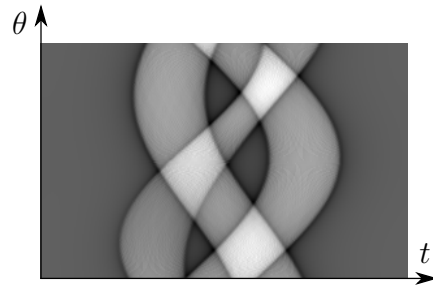
It is easy to see that simple ensemble averaging over multiple realizations μ_{eff}^i



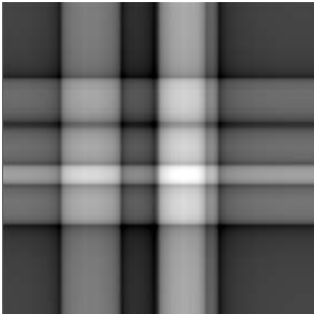
(a)



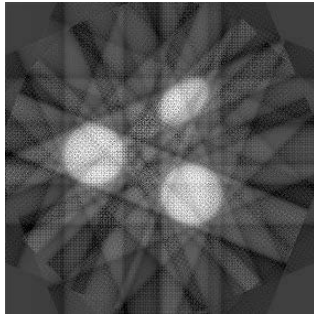
(b)



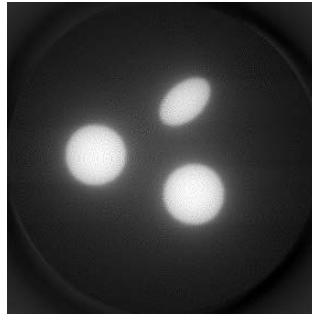
(c)



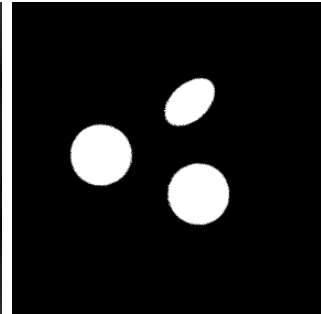
(d)



(e)



(f)



(g)

Figure 2.3: (a) Original sample geometry, (b) projections and (c) filtered projections. (d) Reconstruction with 2 filtered projections at $\theta = 0^\circ$ and $\theta = 90^\circ$, (e) reconstruction with 8 filtered projections, and (f) reconstruction with 180 filtered projections. (g) Denoised and semi-binarized version of (f). Dark and bright colors indicate small and large value of μ_{eff} , p_θ , p'_θ and f in (a, d–f), (b), (c), and (g), respectively.

gives

$$\frac{1}{N} \sum_{i=1}^N \mu_{\text{eff}}^i = \frac{1}{N} \sum_{i=1}^N \mu'_{\text{eff}} + \frac{1}{N} \sum_{i=1}^N n^i \quad (2.19)$$

$$= \mu'_{\text{eff}} + \bar{n}. \quad (2.20)$$

In other words, the undegraded image can be recovered up to an additive constant by averaging multiple degraded images, and the constant \bar{n} is an estimate of the mean of the noise distribution. However, multiple μ_{eff} of the same sample are rarely available, and one must resort to some kind of spatial processing.

The images obtained using X- μ CT are digital, *i.e.* the value of the underlying function μ_{eff} is known at discrete locations that are referred to as pixels. A simple spatial filtering method is averaging over the neighbourhood of a pixel, *i.e.*,

$$\hat{\mu}_{\text{eff}}(\vec{x}) = E(\vec{x}) = \frac{1}{N(\Omega(\vec{x}))} \sum_{\vec{p} \in \Omega(\vec{x})} \mu_{\text{eff}}(\vec{p}), \quad (2.21)$$

where $\hat{\mu}_{\text{eff}}$ is an estimate of μ'_{eff} , $\Omega(\vec{x}) = \{\vec{p} : \|\vec{p} - \vec{x}\| \leq r\}$ is the neighbourhood of position \vec{x} , containing all the pixels that are nearer to \vec{x} than a parameter r , and $N(\Omega(\vec{x}))$ denotes the count of pixels in $\Omega(\vec{x})$. Weighting the pixels of the neighbourhood by a Gaussian function in the distance to the center pixel results in Gaussian filtering, where

$$\hat{\mu}_{\text{eff}}(\vec{x}) = \frac{\sum_{\vec{p} \in \Omega(\vec{x})} G_{\sigma}(\|\vec{x} - \vec{p}\|) \mu_{\text{eff}}(\vec{p})}{\sum_{\vec{p} \in \Omega(\vec{x})} G_{\sigma}(\|\vec{x} - \vec{p}\|)} \approx (G_{\sigma} * \mu_{\text{eff}})(\vec{x}), \quad (2.22)$$

where

$$G_{\sigma}(r) = \frac{1}{\sigma\sqrt{2\pi}} \exp\left(-\frac{r^2}{2\sigma^2}\right), \quad (2.23)$$

and $\Omega(\vec{x})$ must be large enough so that the value of $G_{\sigma}(\|\vec{x} - \vec{p}\|)$ is negligible at the boundary of $\Omega(\vec{x})$.

A disadvantage of simple spatial averaging or Gaussian filtering is the inevitable smoothing of sharp edges. Such blurring can be reduced by, *e.g.*,

weighting the pixel values in the neighbourhood by difference to the value of the center pixel. The weighting results in so-called bilateral filter, where

$$\hat{\mu}_{\text{eff}}(\vec{x}) = \frac{\sum_{\vec{p} \in \Omega(\vec{x})} G_{\sigma}(\|\vec{x} - \vec{p}\|) G_{\tau}(\mu_{\text{eff}}(\vec{x}) - \mu_{\text{eff}}(\vec{p})) \mu_{\text{eff}}(\vec{p})}{\sum_{\vec{p} \in \Omega(\vec{x})} G_{\sigma}(\|\vec{x} - \vec{p}\|) G_{\tau}(\mu_{\text{eff}}(\vec{x}) - \mu_{\text{eff}}(\vec{p}))} \quad (2.24)$$

and G_{τ} is defined analogously to G_{σ} above.

The probability of existence of a sharp edge near \vec{x} can be quantified by comparing the local variance $\sigma(\vec{x})^2$ to the variance of noise σ_{η}^2 , where

$$\sigma(\vec{x})^2 = \frac{1}{N(\Omega(\vec{x}))} \sum_{\vec{p} \in \Omega(\vec{x})} (\mu_{\text{eff}}(\vec{p}) - E(\vec{x}))^2 \quad (2.25)$$

with $N(\Omega(\vec{x}))$ and $E(\vec{x})$ defined as in Equation (2.21). If the local variance at \vec{x} is higher than the variance of noise, it is probable that there is a sharp edge near \vec{x} and thus the image should not be averaged extensively near that location. This idea is formalized in variance-weighted mean filtering, where the ratio of σ_{η}^2 and $\sigma(\vec{x})^2$ is used to decide how much the image should be averaged near \vec{x} [51]. In variance-weighted mean filtering

$$\hat{\mu}_{\text{eff}}(\vec{x}) = \begin{cases} \frac{\sigma_{\eta}^2}{\sigma(\vec{x})^2} E(\vec{x}) + (1 - \frac{\sigma_{\eta}^2}{\sigma(\vec{x})^2}) \mu_{\text{eff}}(\vec{x}), & \sigma_{\eta}^2 \leq \sigma(\vec{x})^2, \\ E(\vec{x}), & \text{otherwise.} \end{cases} \quad (2.26)$$

Also other, more sophisticated filtering methods designed to preserve edges have been suggested, *e.g.* SUSAN smoothing [53], anisotropic diffusion [54], and non-local mean filtering [55]. The common denominator in all of these methods is the effort to perform less averaging near the edges of structures.

The filtering methods discussed above attenuate noise, but do not affect variations of the local mean intensity across the image. Such global bias can be removed based on the observation that Gaussian filtering attenuates variations whose radius is less than σ . By subtracting a Gaussian filtered image from the original, a high-pass filter that removes large variations is

established:

$$\hat{\mu}_{\text{eff}} = \mu_{\text{eff}} - G_{\sigma} * \mu_{\text{eff}}. \quad (2.27)$$

All of the filtering methods discussed above contain one or more parameters, *e.g.* radius of a neighbourhood, standard deviation of a Gaussian function or variance of noise. Often the values of the parameters cannot be qualitatively derived from the image μ_{eff} , and a trial-and-error approach is used instead. The image is filtered using initial values of the parameters and the goodness of the filtering result is evaluated. If the filtering result is inappropriate, the values of the parameters are tuned. The process is repeated until satisfactory results are obtained.

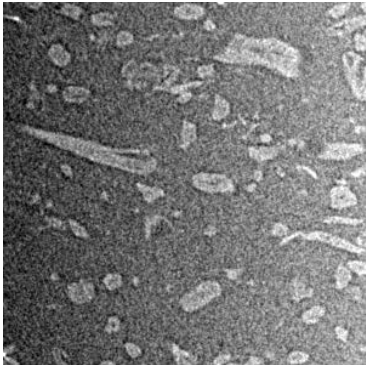
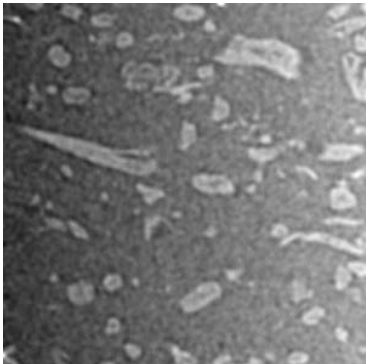
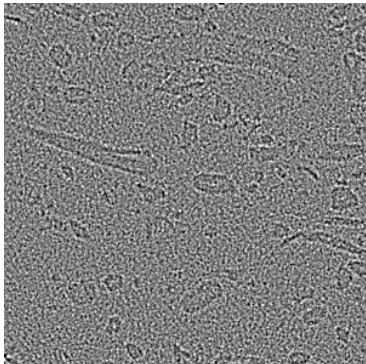
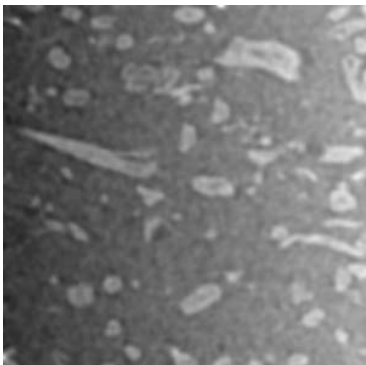
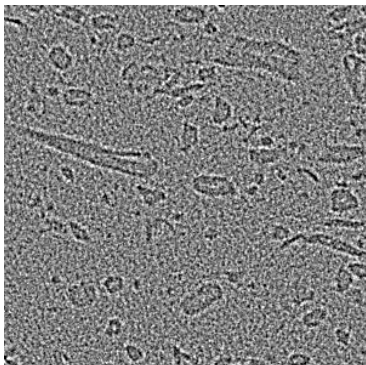
A simple, yet subjective, way to judge between proper and improper filtering is to study the noise that the filtering process removed from the image, *i.e.* the residual $\hat{\mu}_{\text{eff}} - \mu_{\text{eff}}$ [55]. If the residual image seems to contain something else than noise, the filtering operation has probably been improper. The filtering methods discussed above and the corresponding residuals for a test image are visualized in Table 2.1.

The composite materials studied in thesis often contain only two phases of interest, *e.g.*, fibres and matrix. In that case they can be separated from each other by simple mapping

$$f(\vec{x}) = \begin{cases} 0 & \text{if } \hat{\mu}_{\text{eff}}(\vec{x}) < \hat{\mu}_{\text{min}} \\ \frac{\hat{\mu}_{\text{eff}}(\vec{x}) - \hat{\mu}_{\text{min}}}{\hat{\mu}_{\text{max}} - \hat{\mu}_{\text{min}}} & \text{if } \hat{\mu}_{\text{min}} \leq \hat{\mu}_{\text{eff}}(\vec{x}) \leq \hat{\mu}_{\text{max}} \\ 1 & \text{if } \hat{\mu}_{\text{max}} < \hat{\mu}_{\text{eff}}(\vec{x}) \end{cases} \quad (2.28)$$

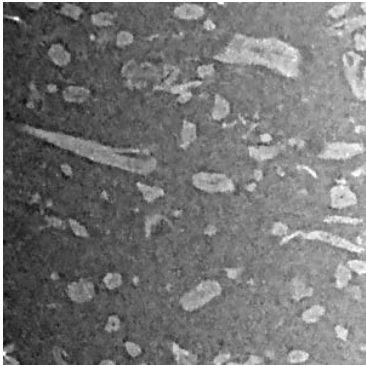
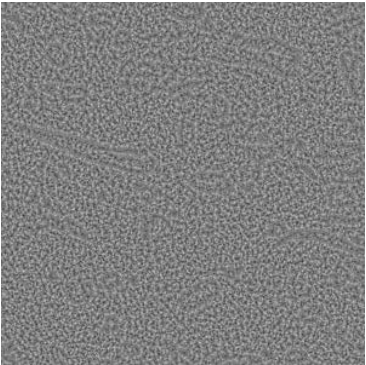
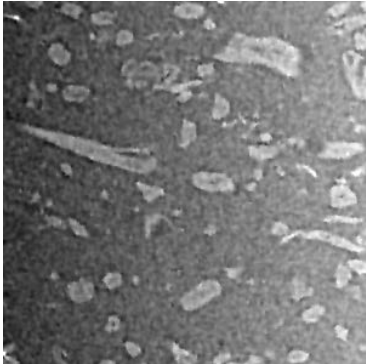
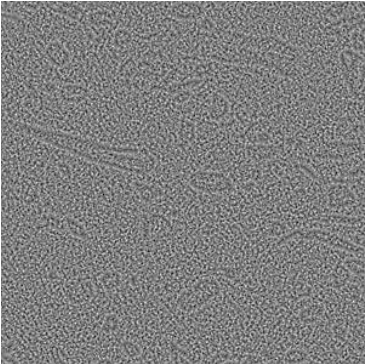
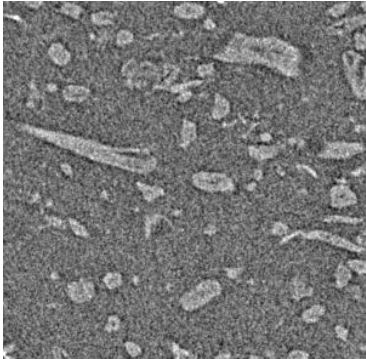
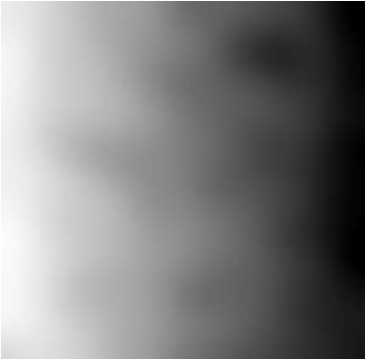
that can be interpreted as a semi-binary image, where $f(\vec{x})$ is identified as the local volume fraction of the denser phase near \vec{x} (see *e.g.* Figure 2.3(g)). The mapping is called thresholding and the function f is called binary image when $\hat{\mu}_{\text{min}} = \hat{\mu}_{\text{max}}$ such that the codomain of f is $\{0, 1\}$. Equation (2.28) can be easily generalized for more than two phases.

Table 2.1: Comparison of filtering methods on an X- μ CT slice through wood fibre – lignin composite [1]. Dynamic range is 1500 gray values in all the $\hat{\mu}_{\text{eff}}$ images, and 700 gray values in all the $\hat{\mu}_{\text{eff}} - \mu_{\text{eff}}$ images. The bright regions in the $\hat{\mu}_{\text{eff}}$ images are cross-sections of wood fibres.

Method, parameters	Estimate $\hat{\mu}_{\text{eff}}$	Residual $\hat{\mu}_{\text{eff}} - \mu_{\text{eff}}$
Original μ_{eff} no filtering		
Mean $r = 2$		
Gaussian $\sigma = 2$		

Continued on next page

Table 2.1: Comparison of filtering methods

Method, parameters	Estimate $\hat{\mu}_{\text{eff}}$	Residual $\hat{\mu}_{\text{eff}} - \mu_{\text{eff}}$
Bilateral $\sigma = 2$ $\tau = 150$		
Variance weighted mean $r = 2$ $\sigma_{\eta} = 150$		
High-pass $\sigma = 40$		

Chapter 3

Characterization of the 3D microstructure of composite materials by image analysis

3.1 Composite materials

The subject of this thesis is fibrous composite materials, *i.e.* composite materials consisting of fibres and some condensed matter as matrix. As the image processing methods presented in the later sections are mainly designed to estimate quantities related to fibres, the subject is limited to such composites where the fibres are short enough such that they approximately fit into the field of view of tomographic image. Hence, the focus is on short-fibre composites and especially on those materials where wood fibres are used as the reinforcing phase.

Wood fibres and many other natural fibres are tubular, *i.e.* a typical, ideal cross-section of the fibre contains a void surrounded by fibre wall. Many image processing algorithms designed for solid fibres cannot be directly applied to hollow fibres. For example, algorithms based on finding the centerline of the fibre may instead find an arbitrary line through the fibre wall, or an algorithm

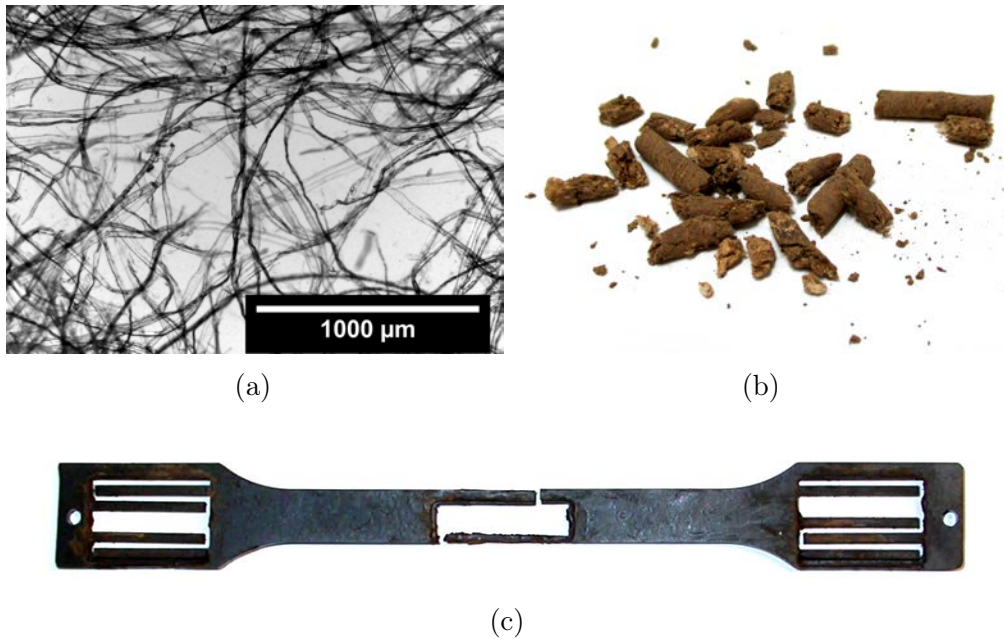


Figure 3.1: (a) Microscopic image of wood pulp fibres. (b) Extruded granulates containing wood fibres and lignin. The diameter of the granulates is approximately 5 mm. (c) Injection moulded tensile test specimen made of wood fibre – lignin composite. The length of the specimen is approximately 17 cm. Parts of the specimen in both ends and in the middle have been cut away into samples for X- μ CT imaging.

for determining the cross-sectional diameter of the fibre may instead find the thickness of fibre wall.

The natural fibre composites studied in this thesis are manufactured using injection moulding technique. The process begins by extraction of fibres from plants using standard processes, *e.g.*, pulping of wood (see Figure 3.1(a)). In the subsequent steps, the fibres are mixed with the matrix material and fed into a moulding device that forms the final product.

Mixing the fibres with the matrix is done either by extruding or by commingling. In the former process, the fibres are first processed into pelletized form using specific equipment. The fibre pellets are mixed with matrix pellets and fed through an extruder and chopper, producing relatively irregular

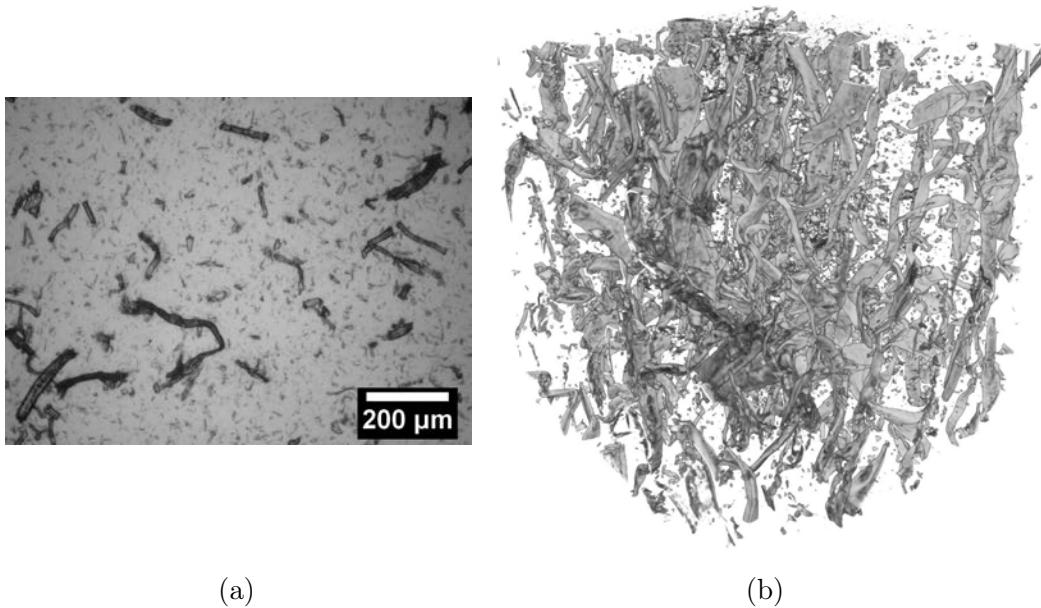


Figure 3.2: (a) Optical micrograph of wood fibres extracted from poly(lactic acid) matrix by dissolution in chloroform [2]. (b) Three-dimensional X- μ CT visualization of fibres in a wood-fibre – poly(lactic acid) composite. Gary Chinga-Carrasco is acknowledged for providing the image in (a).

granulates consisting of fibres and matrix (see Figure 3.1(b)).

Another technique for mixing is commingling, where wood fibres and defibrated matrix are formed into a paper-like sheet where the two kinds of fibres are evenly mixed. The sheet is chopped into small pieces that are fed through an extruder such that the mix forms similar granulates than in the extruding process [3, 8].

After mixing, the granulates are fed into the injection moulding device. The device melts the granulates, mixes them between screws and finally compresses the mix into a mould. The mould shapes the material into the desired form (see Figure 3.1(c)).

In the extruding and moulding processes the fibres must travel through screws, nozzles, and other volumes where shear force and temperature is potentially high. If the durability of the fibres against those harsh conditions is limited, as may be the case with natural fibres, the procedures may change the geometry

of the fibres considerably. As the geometry affects the mechanical properties of the composite material, it is of interest to seek for processing conditions where the fibres survive as intact as possible. Typically the survival of fibres is quantified by fibre length- and fibre diameter distributions.

The traditional method for characterization of fibre geometry is optical microscopy. The matrix material is dissolved [2] or burnt away such that the fibres are left more or less intact. The remaining fibres are collected and placed on glass slides. Optical micrographs (see Figure 3.2(a)) of the fibres are acquired and the geometry of the fibres is characterized either manually or by some image analysis routines. Another possibility is to mix the fibres with suitable liquid and run the suspension through a fibre analyzer (*e.g.* kajaaniFiberLab, Metso Automation OY [56]).

Another method for characterization of fibre shape is microscopy of polished cross-sections [57]. A cross-sectional cut is made into the composite material and the cut surface is polished such that the cross-sections of the fibres are visible. Micrographs of the surface are acquired using optical microscope or scanning electron microscope. The cross-sections of the fibres can then be analyzed from the images as desired. A three-dimensional image can be obtained if the cutting-imaging or polishing-imaging process is repeated many times [13, 14, 16, 17].

The methods above are accurate but laborious. Both of them apply large chemical or mechanical forces to the sample, thus potentially altering the shape of the fibres. The dissolution method also destroys information about the locations of the fibres in the material such that, *e.g.*, fibre orientation and spatial distribution of the volume fraction of fibres are lost. Thus, non-destructive method such as X- μ CT is desirable as it makes unnecessary several processing steps that may increase uncertainties in the analysis process. Additionally, in the X- μ CT image all the information about the structure of the material is recorded, allowing also assessment of the geometrical relations of the individual fibres (Figure 3.2(b)).

In addition to optimization of manufacturing processes, micromechanical

modelling is a discipline where information about the structure of composite material is required. The purpose of micromechanical modelling is to estimate the physical properties of bulk material based on information about its microstructure [4, 7, 58]. Typical quantities that are required in a micromechanical model are volume fractions of different constituents, length and diameter of fibres and their orientation distribution, all of which can be measured from X- μ CT images. The X- μ CT images could also be used to provide a grid geometry for numerical simulations as has been done in the field of flow analysis [59, 60].

3.2 General structural properties

In the semi-binary image formalism (see Section 2.2.3), an estimate of the volume fraction of fibres ϕ_f is obtained by taking an average over the values of the pixels of the semi-binary image,

$$\phi_f = \frac{1}{N} \sum_i f_i, \quad (3.1)$$

where f is the semi-binary image of fibres and the sum is taken over all the N pixels.

Variations in the local volume fraction are indicative of the dispersion of the fibres in the matrix. An estimate of the local volume fraction is developed by replacing the sum in Equation (3.1) by a sum over a local neighbourhood $\Omega(\vec{x})$ of point \vec{x} ,

$$\phi_f(\vec{x}) = \frac{1}{N(\Omega(\vec{x}))} \sum_{\vec{p} \in \Omega(\vec{x})} f(\vec{p}), \quad (3.2)$$

where $N(\Omega(\vec{x}))$ denotes the count of pixels in the neighbourhood $\Omega(\vec{x})$ as in Equation (2.21). The variations in $\phi_f(\vec{x})$ may then be studied, *e.g.*, from the distribution of values $\phi_f(\vec{x})$ obtained by statistical binning over all \vec{x} .

Another possibility to quantify the dispersion of the fibres is the distribution of inter-fibre distance. Following definition of local thickness in Hildebrand

and Rügsegger [19], inter-fibre distance $d(\vec{x})$ at point \vec{x} is the diameter of the largest sphere that fits into the matrix and contains the point \vec{x} . Statistical binning of $d(\vec{x})$ over all points in the matrix can be used to determine the inter-fibre distance distribution of matrix volume (Figure 3.4).

The local thickness is defined for binary images only. A method for determining inter-fibre distance $d(x)$ from semi-binary images is granulometry [51]. It is based on removing small matrix structures from the image based on a specific size criterion, and recording the volume of the remaining structures. Repeating the process by removing matrix structures of increasing size gives the unnormalized complementary cumulative size distribution of matrix volume. The process is analogous to sieving by a series of sieves with increasing hole size and determining the amount of material that remains in each sieve.

In granulometry, the removal of small structures is performed by opening operation that consist of erosion followed by dilation. Given a semi-binary image g and a structuring element function b , dilation of g by b is defined as

$$(g \oplus b)(\vec{x}) = \max\{g(\vec{x} - \vec{r}) + b(\vec{r})\} \quad (3.3)$$

where the maximum is taken over all \vec{r} . Similarly, erosion of g by b is defined as

$$(g \ominus b)(\vec{x}) = \min\{g(\vec{x} + \vec{r}) - b(\vec{r})\}. \quad (3.4)$$

Finally, the opening of g by b is defined as

$$(g \circ b)(\vec{x}) = ((g \ominus b) \oplus b)(\vec{x}). \quad (3.5)$$

The effect of erosion and opening operations on a one-dimensional function is demonstrated in Figure 3.3. In the example, the original function g consist of a narrow bump and a wide bump. The structuring element b is a one-dimensional sphere whose radius is 0.05, *i.e.*

$$b(x) = \mathcal{B}_{0.05}(x) = \begin{cases} 0, & -0.05 < x < 0.05, \\ -\infty, & \text{otherwise.} \end{cases} \quad (3.6)$$

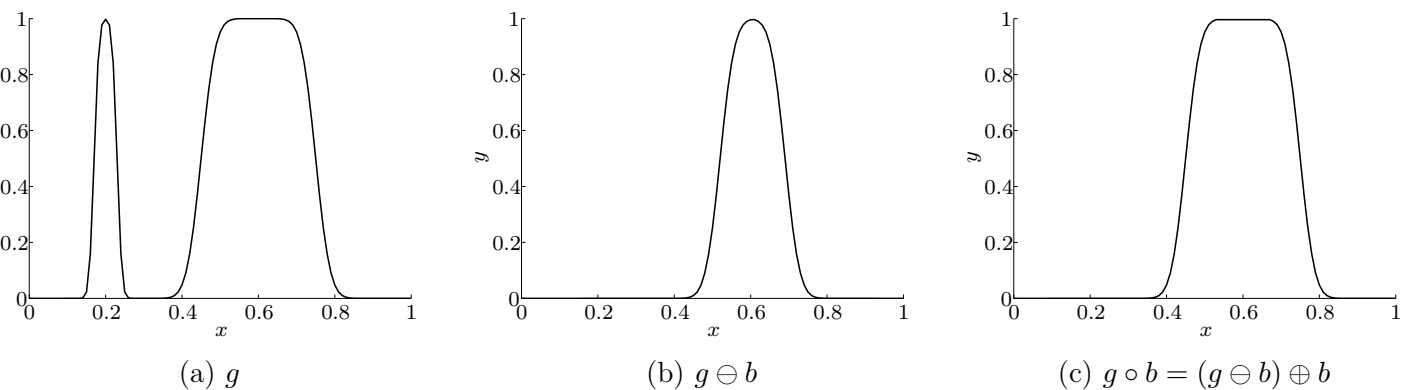


Figure 3.3: Demonstration of opening of one-dimensional function g by b , where $b(x) = 0$ when $-0.05 < x < 0.05$ and $-\infty$ otherwise. (a) Original function g , (b) erosion of g by b and (c) opening of g by b . Notice that the narrow bump at $x = 0.2$ is removed but the wide bump at $x = 0.6$ is retained.

In the erosion of g by b the narrow bump is completely zeroed and the size of the wide bump is decreased. Dilation by the same structuring element restores the size of the wider bump but the narrow bump is still missing, as it was completely removed in the erosion phase. Roughly speaking, opening of g by \mathcal{B}_r is g with those locations zeroed where \mathcal{B}_r does not fit.

Based on the above example, it is easy to see that for a semi-binary image g , the total volume of structures locally thicker than diameter $d = 2r$ is given by

$$V(d) = V_1 \sum_i (g \circ \mathcal{B}_r)_i, \quad (3.7)$$

where V_1 is the volume of a single pixel (compare to Equation (3.1)). Normalizing Equation (3.7) by its maximal value gives the cumulative diameter distribution of volume as

$$P(d) = 1 - \frac{\sum_i (g \circ \mathcal{B}_r)_i}{\sum_i g_i}. \quad (3.8)$$

Differentiation of both sides yields the probability density function

$$p(d) = -\frac{\partial}{\partial d} \frac{\sum_i (g \circ \mathcal{B}_r)_i}{\sum_i g_i}, \quad (3.9)$$

which can be interpreted as the diameter distribution of g . Further, defining $g = 1 - f$, $p(d)$ becomes an estimate of the diameter distribution of inter-fibre space. Alternatively, defining $g = f$ gives the diameter distribution of fibres or fibre walls for solid or hollow fibres, respectively.

Figure 3.4 shows the results of calculating diameter distribution of a triangle using both the local thickness algorithm of Hildebrand and Rügsegger [19] and the granulometry as discussed above. Based on the figure, it is evident that the two methods give similar estimates in this case. The algorithm in [19] is computationally less demanding, in general. On the other hand, the granulometry algorithm is relatively easy to adjust to fit into specific situations, as will be demonstrated later.

The local orientation can be determined using the structure tensor method [21]. The structure tensor is defined for each point in an image f as

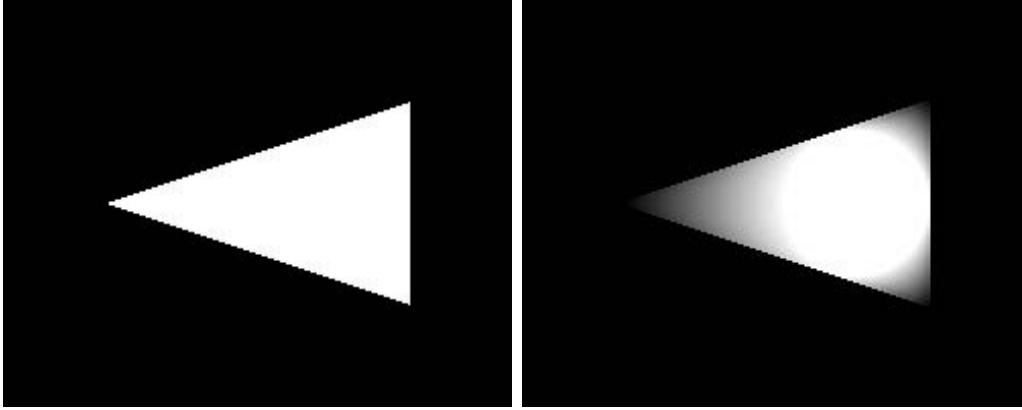
$$S_{ij} = G_{\sigma_t} * \left(\frac{\partial f}{\partial x_i} \frac{\partial f}{\partial x_j} \right), \quad (3.10)$$

where G_{σ_t} is a Gaussian function defined in Equation (2.23). By doing a Gaussian pre-smoothing on the image, the partial derivatives can be approximated by

$$\frac{\partial f(\vec{x})}{\partial x_i} \approx \frac{\partial}{\partial x_i} (G_{\sigma_s} * f)(\vec{x}) = \left(\frac{\partial G_{\sigma_s}}{\partial x_i} * f \right) (\vec{x}). \quad (3.11)$$

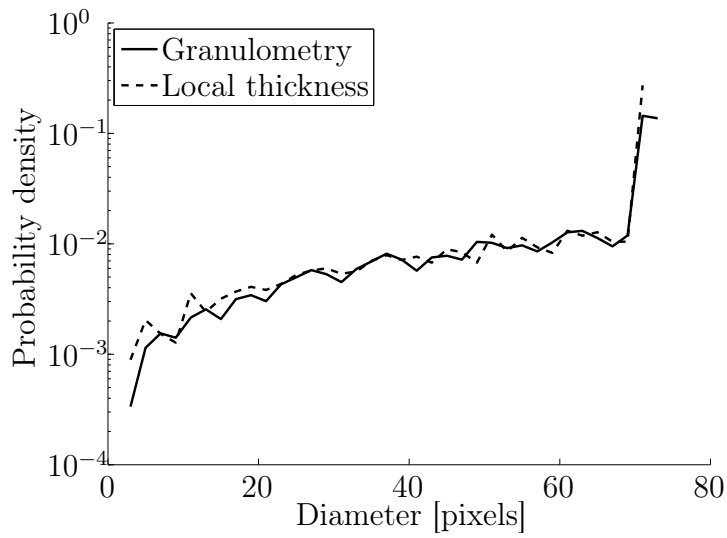
Finally, the orientation of fibres near \vec{x} is given by the eigenvector of $S_{ij}(\vec{x})$ corresponding to the smallest eigenvalue.

The interpretation of S_{ij} can be demonstrated by considering a neighbourhood in a two-dimensional image containing a linear ramp of values in direction $\nabla f = (c_1, c_2)$, see Figure 3.5. In that case, the eigenvalues (λ_1, λ_2) and



(a)

(b)



(c)

Figure 3.4: Comparison between results of granulometry and local thickness methods. (a) The original image, (b) its diameter map and (c) the diameter distribution of area estimated using the two methods. In (b), black and white colors correspond to diameters of 0 and 71 pixels, respectively.

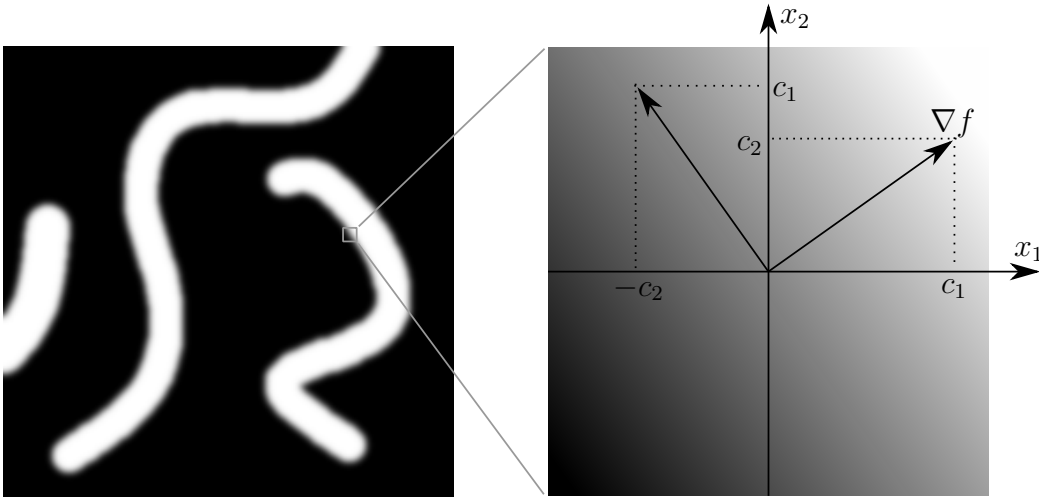


Figure 3.5: Determination of local orientation in two-dimensional image. The local neighbourhood contains a gradient, whose direction is determined by eigenvector (c_1, c_2) of the structure tensor.

-vectors (\vec{v}_1, \vec{v}_2) of S_{ij} are

$$\lambda_1 = 0, \quad \vec{v}_1 \propto \begin{pmatrix} -c_2 \\ c_1 \end{pmatrix} \quad (3.12)$$

$$\lambda_2 = c_1^2 + c_2^2, \quad \vec{v}_2 \propto \begin{pmatrix} c_1 \\ c_2 \end{pmatrix}. \quad (3.13)$$

The eigenvector corresponding to the largest eigenvalue, \vec{v}_2 , is parallel with the gradient vector. If the gradient represents, *e.g.*, interface between an object and the background, the vector \vec{v}_2 estimates the direction of the normal of the interface. On the other hand, \vec{v}_1 estimates direction of the tangent of the interface. The estimates are robust in the sense that negating the direction of the gradient does not affect the eigenvectors.

Consider now a three-dimensional local neighbourhood containing a small part of the wall of a cylinder. In that case the eigenvector corresponding to the largest eigenvalue is parallel with the normal of the cylinder wall. The eigenvector corresponding to the smallest eigenvalue is parallel with the direction of the main axis of the cylinder.

The above example generalizes to the case of fibres in composite materials. The fibres are long structures and resemble cylinders, whose local orientation can be determined as the eigenvector corresponding to the smallest eigenvalue of the structure tensor. However, it must be noted that this kind of orientation estimate is valid only near the surfaces of the fibres and should, in particular, be regarded as the orientation of the fibre surfaces. Consequently, the distribution of local orientation determined using the structure tensor method does not necessarily coincide with the orientation distribution of individual fibres.

3.3 Properties of dispersed particle phase

In this section, the term 'particle' refers to any object of interest in an image. The particle may be, *e.g.*, a fibre in a three-dimensional X- μ CT image or a cross-section of a fibre in a two-dimensional image of a polished cross-section of a composite material sample. It is assumed that the particles are not connected to each other and are thus seen as separate regions in the image. Furthermore, the treatment in this section is limited to binary images f , where

$$f(\vec{x}) = \begin{cases} 1, & \text{if } \vec{x} \text{ is inside a particle and} \\ 0, & \text{otherwise.} \end{cases} \quad (3.14)$$

Given a binary image of particles that are not connected to each other, the pixels belonging to each particle can be determined with labeling algorithms [61]. A labeling algorithm, such as that in Algorithm 1, assigns a distinct value to each particle such that all the pixels belonging to the same particle have the same value.

Consider one of the particles in an n -dimensional image and denote by column vectors \vec{x}_i , $i = 1, \dots, m$ the positions of the pixels of the particle. The volume of the particle is given by

$$V = mV_1, \quad (3.15)$$

where V_1 is the volume of a single pixel.

Algorithm 1 Labeling algorithm

Input: Binary image f , where pixels belonging to any particle have value 1 and other pixels have value 0.

Output: Image f where pixels belonging to a single particle have equal value and pixels belonging to different particles have distinct values.

```
1: Initialize  $E \leftarrow \{\vec{x} : f(\vec{x}) = 1\}$ 
2: Initialize current label  $c \leftarrow 2$ 
3: for all  $\vec{x} \in E$  do
4:   if  $f(\vec{x}) = 1$  then
5:     FLOODFILL( $f, \vec{x}, c$ )
6:      $c \leftarrow c + 1$ 
7:   end if
8: end for
9: return  $f$ 
```

```
10: function FLOODFILL( $f, \vec{x}, c$ )
11:   Initialize  $t \leftarrow f(\vec{x})$ 
12:   Initialize  $Q \leftarrow \{\vec{x}\}$ 
13:   while  $Q \neq \emptyset$  do
14:      $\vec{x} \leftarrow$  some element of  $Q$ 
15:      $Q \leftarrow Q \setminus \{\vec{x}\}$ 
16:     if  $f(\vec{x}) = t$  then
17:        $f(\vec{x}) \leftarrow c$ 
18:        $Q \leftarrow Q \cup \Omega(\vec{x})$ 
19:     end if
20:   end while
21: end function
```

The surface area of the particle may be approximated, *e.g.*, by the marching cubes algorithm [62, 63]. Consider a binary image h defined by

$$h(\vec{x}) = \begin{cases} 1, & \vec{x} \in \{\vec{x}_i, i = 1, \dots, m\} \\ 0, & \text{otherwise.} \end{cases} \quad (3.16)$$

The image h is first divided into separate blocks of size $2 \times 2 \times \dots \times 2 = 2^n$ pixels, where n is the dimensionality of the image. As each pixel in a block has two possible values (either zero or one), there are 2^{2^n} possible pixel value configurations for a single block. Each configuration corresponds to a location

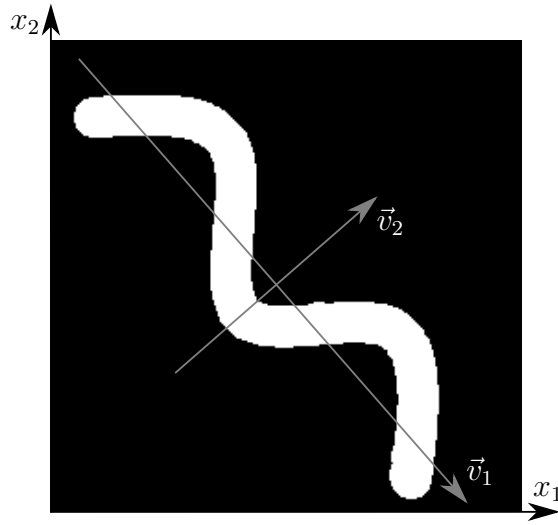


Figure 3.6: Principal component analysis for determination of fibre orientation. The white area depicts a fibre. The vectors \vec{v}_1 and \vec{v}_2 are parallel to the principal components of the fibre. The first principal component \vec{v}_1 estimates the orientation of the fibre.

either completely inside the particle, completely outside of it or at the edge between the particle and the background. Each of the configurations has a pre-calculated surface area associated with it, determined analytically or by numerical simulations. To estimate the surface area of the particle, the configuration of pixel values in each block is determined and the corresponding surface area is looked up from a pre-calculated table. The surface areas corresponding to the blocks are then summed, giving an estimate of the surface area of the particle.

The marching cubes algorithm has the drawback of not being multigrid convergent, *i.e.*, the result of the algorithm does not necessarily converge to the true value of the surface area as the resolution of the image is increased. In the cases encountered in this thesis the error is not significant, but it is worth to mention that several multigrid convergent algorithms have been developed [64, 65].

The orientation of the particle can be determined with principal component analysis [66]. The first principal component of $\{\vec{x}_i, i = 1, \dots, m\}$ is \vec{v}_1 that

satisfies

$$\vec{v}_1 = \arg \max_{\vec{u}, \|\vec{u}\|=1} \sum_{i=1}^m ((\vec{x}_i - \vec{\mu}) \cdot \vec{u})^2, \quad (3.17)$$

where the mean vector $\vec{\mu}$ is given by

$$\vec{\mu} = \frac{1}{m} \sum_{i=1}^m \vec{x}_i. \quad (3.18)$$

In other words, the \vec{v}_1 is the unit vector for which the variance of the scalar projections $(\vec{x}_i - \vec{\mu}) \cdot \vec{v}_1$ is maximal. The second and higher principal components have similarly maximal projected variance but under the constraint that their direction is orthogonal to all the previous principal components. Thus, principal component analysis gives an orthogonal coordinate system where the first axis estimates the direction of the particle, see Figure 3.6.

To conveniently determine the principal components, we begin by forming an $n \times m$ data matrix

$$\mathbf{X} = \begin{pmatrix} \vec{x}_1 - \vec{\mu} & \vec{x}_2 - \vec{\mu} & \dots & \vec{x}_m - \vec{\mu} \end{pmatrix}. \quad (3.19)$$

The $n \times n$ covariance matrix \mathbf{C} is given by

$$\mathbf{C} = \frac{1}{m} \mathbf{X} \mathbf{X}^T \quad (3.20)$$

and its eigenvectors are the principal components of \vec{x}_i . The eigenvector corresponding to the largest eigenvalue is the first principal component, the eigenvector corresponding to the second largest eigenvalue is the next principal component etc.

The convex hull of the particle is the smallest convex set that contains all the points $\{\vec{x}_i, i = 1, \dots, m\}$ of the particle. As the set of points is discrete, the boundary of the convex hull can be expressed as a set of triangular faces. The faces can be determined using, *e.g.*, the gift-wrapping algorithm [67]. In the three-dimensional case the algorithm is outlined as follows.

1. Denote by $\{\vec{y}_i, i = 1, \dots, m\}$ projections of points $\{\vec{x}_i, i = 1, \dots, m\}$

to the xy -plane. Find a point \vec{y}_j with minimum y -coordinate. Find a point \vec{y}_k such that

$$(\vec{y}_k - \vec{y}_j)^\perp \cdot (\vec{y}_l - \vec{y}_j) \geq 0 \quad (3.21)$$

for all l , where \vec{A}^\perp denotes \vec{A} rotated 90° counterclockwise. Add line $\vec{x}_j\vec{x}_k$ to a set of edges.

2. Take an unprocessed edge $\vec{x}_j\vec{x}_k$ from the set of edges. Find a point \vec{x}_l such that

$$(\vec{x}_l - \vec{x}_j) \times (\vec{x}_k - \vec{x}_j) \cdot (\vec{x}_l - \vec{x}_j) \geq 0 \quad (3.22)$$

for all i . Add edges $\vec{x}_k\vec{x}_l$ and $\vec{x}_l\vec{x}_j$ to the set of edges if they have not been added to it before. Add a triangle $\vec{x}_j\vec{x}_k\vec{x}_l$ to the boundary of the convex hull.

3. Repeat step 2 until no edges can be processed.

The triangles forming the boundary of the convex hull may be used to determine, *e.g.*, the surface area or the volume of the convex hull. In particular, convex particles can be separated from concave ones by studying the value of

$$C = \frac{V_C}{V}, \quad (3.23)$$

where V_C is the volume of the convex hull and V is the volume of the particle (see also Section 4.2).

In order to quantify voids or cavities in a particle, pixels belonging to each cavity must be determined. Consider a binary image g defined by

$$g(\vec{x}) = \begin{cases} 0, & \vec{x} \in \{\vec{x}_i, i = 1, \dots, m\} \\ 1, & \text{otherwise.} \end{cases} \quad (3.24)$$

The value of g is one in all the cavities inside the original particle and in the background around the original particle. The image g thus contains cavities and background as new non-connected particles that can be labeled and analyzed with the methods discussed above. The results corresponding to the background can be discarded by noticing that the background is the

only such particle that touches the edge of the image g .

3.4 Properties of interconnected particle phase

For interconnected particles, the methods of Section 3.3 cannot be used unless the individual particles are identified from each other. In the context of composite materials the particles are often fibres. Several attempts for identifying individual fibres from each other have been recently made [22–28, 30–33, 35]. The identification methods are applicable if the structure of the fibres is regular or if the fibres form a layered network structure whose properties can be utilized in the identification process.

Natural fibres, on the other hand, have more irregular structure than, *e.g.*, glass fibres. Additionally, processing may crush the fibres such that their shape becomes highly irregular, *e.g.*, partially solid and partially hollow. The irregular shape hinders application of identification algorithms. Thus, in this section methods will be proposed for estimating properties of fibres without identification of individual fibres.

3.4.1 Fibre length

In Section 3.2, granulometry was presented as a method to estimate the diameter distribution of structures in a semi-binary image without segmentation of individual objects. In granulometry, structures smaller than a given size are removed from the image using an opening operation. In the opening operation, all the structures where the structuring element does not fit are zeroed. Thus, by using a suitable structuring element, granulometry can be applied in estimating the length of structures instead of their diameter.

Traditionally, length has been estimated using a linear structuring element consisting of a thin line with predefined length and orientation [68]. An opening by a linear structuring element is dependent on the orientation of the structuring element. To overcome the orientation dependency one must

consider openings with linear structuring elements in all possible orientations. If any of the openings is nonzero at some location, at least one of the structuring elements fits into the structure at that location. It thus turns out that pointwise maximum of the openings has nonzero value only where there are structures where some of the structuring elements fit. In other words, the points with nonzero value belong to structures whose size in some direction is larger than or equal to the length of the linear structuring elements.

Such a composite operation consisting of pointwise maximum of openings can be used to estimate the length of fibres with granulometry process as in Section 3.2. Theoretically, pointwise maximum of openings with varying structuring elements can still be considered as an opening, although no single structuring element can be associated with it [20, 68, 69].

The practical usability of a method taking a maximum of a large number of openings is limited. To achieve rotationally invariant estimator, the count of orientations of structuring elements must be increased linearly with respect to line length in two-dimensional images, and quadratically in three-dimensional images, leading to unreasonable computational complexity. The problem can be partially overcome by using path openings [70], where the structuring element is a flexible line that is fitted into the fibre pixels.

Path openings

To facilitate definition of a path through pixels in a binary image, let us write $\vec{x} \mapsto \vec{y}$ if pixel at \vec{y} is adjacent to pixel at \vec{x} in such a manner that a path starting at \vec{x} can continue at \vec{y} . Given a binary image of fibres, define E as the set of positions of all fibre pixels. A path of length L in E is denoted by δ_L and is defined as a set of positions $\{\vec{a}_1, \dots, \vec{a}_L\}$ where $\vec{a}_i \mapsto \vec{a}_{i+1}$ for $i = \{1, \dots, L - 1\}$ and $\vec{a}_j \in E$ for $j = \{1, \dots, L\}$.

By choosing the adjacency of pixels appropriately, paths of different orientations can be constructed. For the purposes of length measurement it is beneficial to construct paths that cannot turn back into the direction where

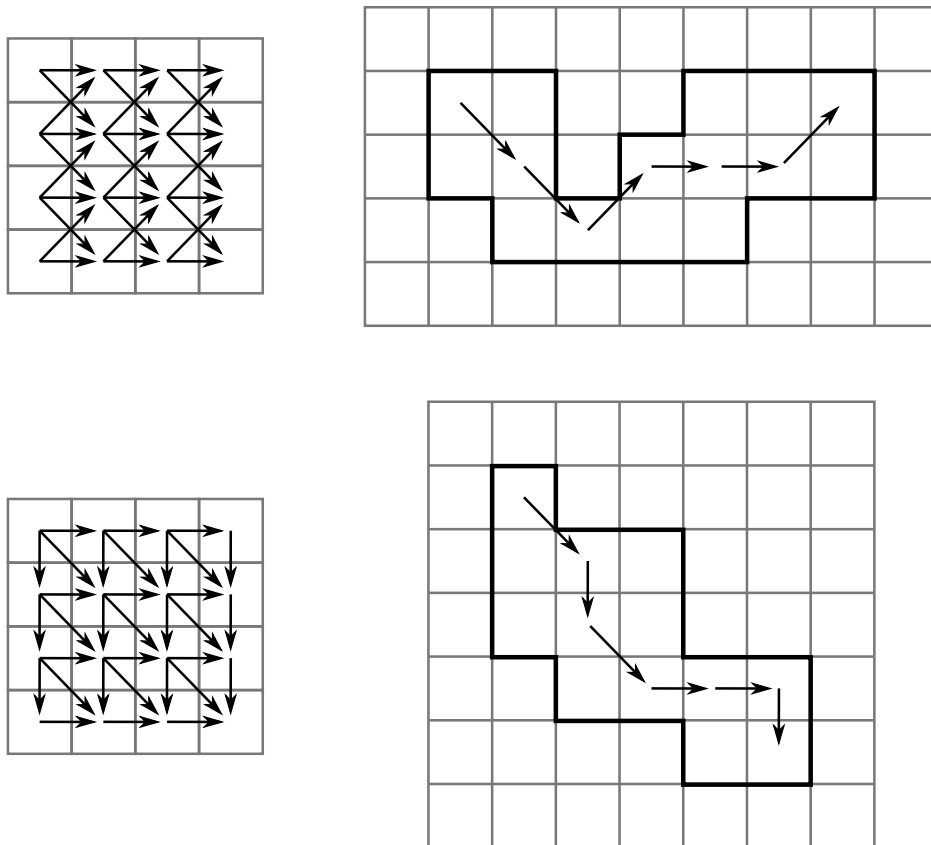


Figure 3.7: Left: Graphs of two adjacency relations, west-to-east (top) and northwest-to-southeast (bottom). The arrows are drawn from each pixel to all adjacent pixels. Right: Examples of arbitrary paths corresponding to the adjacency relations at left, marked with arrows. The boundary of the set E is highlighted.

they came from. As all the positions in a path must be contained in E , the existence of such a directed path through a pixel can be used as an indication that the length of E must be at least the length of the path.

For example, to construct a path from west to east in a two-dimensional image, the adjacency of pixels must be chosen so that pixels at $\vec{x} + (1, -1)$, $\vec{x} + (1, 0)$ and $\vec{x} + (1, 1)$ are adjacent to pixel at \vec{x} , as visualized in the top row of Figure 3.7. In two-dimensional images there are a total of four natural adjacency relations that can be used to form directed paths, characterized by their main directions north-to-south, west-to-east, northwest-to-southeast, southwest-to-northeast. Two of these are visualized in Figure 3.7. In three-dimensional images there are 13 natural adjacency relations.

A path opening of a binary image I is a binary image α_L , where [71]

$$\alpha_L(\vec{x}) = \begin{cases} 1, & \vec{x} \in \bigcup \delta_L \\ 0, & \text{otherwise.} \end{cases} \quad (3.25)$$

In other words, $\alpha_L(\vec{x}) = 1$ if there are any paths of length L going through the point \vec{x} in I , and zero otherwise. As shown in Heijmans et al. [71], α_L or pointwise maximum of multiple α_L can be used in the place of opening in a granulometry.

Talbot and Appleton [72] introduces an algorithm to compute the path opening using an opening transform. Opening transform assigns to each pixel the length of the longest path through it. The pixels that would be nonzero in a path opening with path length L are those whose value in the opening transform is greater than or equal to L . The length distribution of fibre volume is the distribution of values of the opening transform.

For a single adjacency relation, the opening transform can be calculated with a dynamic programming method (see Algorithm 2). Two temporary images, λ^+ and λ^- , are required. The value of λ^+ at \vec{x} is the length of the longest path beginning at \vec{x} and, correspondingly, $\lambda^-(\vec{x})$ is the length of the longest path ending at \vec{x} . The total length of the longest path through \vec{x} is

$\lambda^+(\vec{x}) + \lambda^-(\vec{x}) - 1$. In the algorithm, λ^+ and λ^- are calculated one-by-one as follows.

First, λ^+ is initialized such that $\lambda^+(\vec{x}) = 0$ for all \vec{x} . The pixels of the image are processed in such an order that if $\vec{x} \mapsto \vec{y}$, then \vec{x} is processed before \vec{y} . At each pixel, the value of λ^+ is calculated as

$$\lambda^+(\vec{x}) = \begin{cases} 1 + \max_{\vec{y} \mapsto \vec{x}} \lambda^+(\vec{y}), & \vec{x} \in E, \\ 0, & \text{otherwise.} \end{cases} \quad (3.26)$$

The temporary image λ^- is calculated similarly but by inverting the processing order of pixels and the adjacency relation in the maximum operation.

To finally determine the opening transform, the above algorithm is run for all the relevant adjacency relations and a pointwise maximum of the results is taken.

The above definitions and algorithms are given for binary images only. Path opening for a semi-binary image can be calculated by means of threshold decomposition [72]. The opening of a semi-binary image is determined by first thresholding the image to binary form by threshold level t . The path opening is then calculated for the thresholded image with Algorithm 2 as above. The process is repeated for all values of t and each pixel is assigned the highest value of t for which the corresponding value of the binary opening is nonzero.

Constrained path openings

An apparent problem in using simple path openings for measuring length of structures is zig-zagging, *i.e.* a long path can fit into a short structure by forming a zig-zag pattern. For example, consider a straight two-pixel wide line from west to east. In addition to straight paths, the west-to-east adjacency relation allows also paths consisting of repeated {north-east, south-east}-steps, leading to over-estimation of the length of the structure (see also Figure 3.7). The problem can be partially overcome by constrained path-

Algorithm 2 Opening transform algorithm

Input: Binary image f

Output: Opening transform P of f

```
1: Initialize  $\Psi \leftarrow$  relevant adjacency relations
2: Initialize  $P \leftarrow 0$ 
3: Initialize  $E \leftarrow \{\vec{x} : f(\vec{x}) \neq 0\}$ 
4: for all Adjacency relation  $R \in \Psi$  do
5:    $\lambda^+ \leftarrow \text{CREATELAMBDA}(E, R)$ 
6:    $\lambda^- \leftarrow \text{CREATELAMBDA}(E, -R)$ 
7:    $P \leftarrow \max(P, \lambda^+ + \lambda^- - 1)$ 
8: end for
9: return  $P$ 

10: function CREATELAMBDA( $E, R$ )
11:   Initialize  $\lambda \leftarrow 0$ 
12:   for all Pixel  $\vec{x} \in \text{sort}(E, R)$  do
13:      $\lambda(\vec{x}) \leftarrow 1 + \max_{\vec{y}R\vec{x}} \lambda(\vec{y})$ 
14:   end for
15:   return  $\lambda$ 
16: end function
```

openings where every other step of the path must be in the main direction of the adjacency relation (*i.e.* east for west-to-east adjacency) [70].

The implementation of a constrained opening transform algorithm is based on an observation that a path that has not proceeded to its main direction has to do so in the next step. The count of paths ending (or starting) at a single pixel increases compared to the non-constrained case. In addition to the path that has arrived to the present pixel from any direction, there is also a path that has arrived to the present pixel from the main direction. Hence, we define

- $\lambda_c^-(\vec{x})$ as the length of longest path that ends at \vec{x} and has arrived to \vec{x} from the main direction,
- $\lambda_c^+(\vec{x})$ as the length of longest path that begins at \vec{x} and continues from \vec{x} in the main direction,
- $\lambda^-(\vec{x})$ as the length of longest path that ends at \vec{x} and has arrived to

Algorithm 3 Constrained opening transform algorithm

Input: Binary image f

Output: Constrained opening transform P of f

```
1: Initialize  $\Psi \leftarrow$  relevant adjacency relations and main directions
2: Initialize  $P \leftarrow 0$ 
3: Initialize  $E \leftarrow \{\vec{x} : f(\vec{x}) \neq 0\}$ 
4: for all Adjacency relation  $R$  and main direction  $\vec{v} \in \Psi$  do
5:    $\lambda^+, \lambda_c^+ \leftarrow \text{CREATELAMBDA}(E, R, \vec{v})$ 
6:    $\lambda^-, \lambda_c^- \leftarrow \text{CREATELAMBDA}(E, -R, -\vec{v})$ 
7:    $P \leftarrow \max\{P, \lambda_c^+(\vec{x}) + \lambda^-(\vec{x}) - 1, \lambda^+(\vec{x}) + \lambda_c^-(\vec{x}) - 1\}$ 
8: end for
9: return  $P$ 

10: function CREATELAMBDA( $E, R, \vec{v}$ )
11:   Initialize  $\lambda \leftarrow 0$ 
12:   Initialize  $\lambda_c \leftarrow 0$ 
13:   for all Pixel  $\vec{x} \in \text{sort}(E, R)$  do
14:      $\lambda_c(\vec{x}) \leftarrow 1 + \lambda(\vec{x} - \vec{v})$ 
15:      $\lambda(\vec{x}) \leftarrow 1 + \max_{\vec{y} R \vec{x}} \lambda_c(\vec{y})$ 
16:   end for
17:   return  $\lambda, \lambda_c$ 
18: end function
```

\vec{x} from any direction and

- $\lambda^+(\vec{x})$ as the length of longest path that begins at \vec{x} and continues from \vec{x} to any direction.

The longest constrained path through \vec{x} is

$$\max\{\lambda_c^+(\vec{x}) + \lambda^-(\vec{x}), \lambda^+(\vec{x}) + \lambda_c^-(\vec{x})\} - 1. \quad (3.27)$$

The temporary images λ_c^\pm and λ^\pm are determined as in the non-constrained path transform in Algorithm 2, except that in each iteration step the constrained length must be determined based on non-constrained length and vice versa, as is also shown in Algorithm 3.

3.4.2 Multivariate size distributions

Having determined the length- (Section 3.4.1) and wall thickness (Section 3.2) distributions of fibres separately, let us assess also the correlations of the two distributions. To that end, recall that opening operation by a structuring element b_1 removes all structures where b_1 does not fit. Thus, the size distribution of the remaining structures, with respect to structuring element b_2 , can be estimated with granulometry on opening by structuring element b_1 . By choosing the two structuring elements appropriately, a bivariate size distribution is obtained.

In Miettinen et al. [2] and Miettinen and Kataja [6] such a method was used to determine the bivariate length-diameter distribution of wood fibres in a biodegradable composite material. The volume of particles whose longest dimension is less than L and smallest dimension is less than D was written as

$$V(L, D) = \int S(P(f, L), D) d\vec{x}, \quad (3.28)$$

where $S(f, D)$ is an opening with a spherical structuring element (Section 3.2) and $P(f, L)$ is a constrained path opening (Section 3.4.1). On the other hand, if the volume of a single fibre is given by $V_1(L, D)$, the volume V can be written as

$$V(L, D) = \int_0^L \int_0^D n(L, D) V_1(L, D) dD dL, \quad (3.29)$$

where $n(L, D)$ is the bivariate distribution of number of fibres with respect to L and D . Differentiation gives

$$n(L, D) = \frac{1}{V_1(L, D)} \frac{\partial^2 V(L, D)}{\partial L \partial D}, \quad (3.30)$$

that is the desired result. The problem in the present formulation is that it may not be possible to formulate the volume of a single fibre, V_1 , as a function of L and D . For example, for fibres that have a lumen D corresponds to the thickness of fibre wall. To formulate V_1 one has to, *e.g.*, assume that all

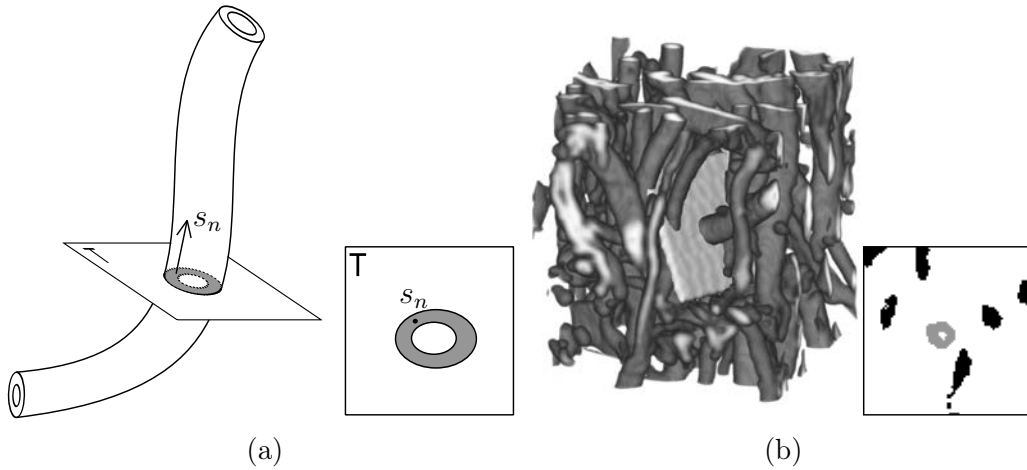


Figure 3.8: (a) Slicing a single fibre. Slice \mathbb{T} is taken such that its normal \hat{s}_n is parallel with the local fibre orientation vector. (b) Small part of X- μ CT image of a composite material. A slice taken from the shaded region is shown in the inset. [1, 7]

fibres in the present material are geometrically similar such that

$$V_1(L, D) \propto LD^2, \quad (3.31)$$

which may not always be appropriate, especially for many natural fibres.

The assumption (3.31) has been relaxed in Miettinen et al. [1] and in Miettinen et al. [7], where another method for determination of cross-sectional properties of fibres has been proposed. The basic idea of the method is to use the constrained path transform for determination of fibre length but to assess the cross-sectional properties of fibres by slicing them based on information on their orientation.

Begin by sampling the image f at random locations such that N points \vec{x}_n inside the fibre phase are found. At each of the points, the local fibre orientation is determined using the structure tensor method as described in Section 3.2. A slice around \vec{x}_n is extracted such that the normal of the slice is parallel with the local fibre orientation vector. Consequently, a cross-section of the fibre containing \vec{x}_n is visible near the center of the extracted slice, as visualized in Figure 3.8. Desired geometrical properties of the fibre cross-

section may then be determined from the two-dimensional slice using, *e.g.*, techniques discussed in Section 3.3.

The length of the fibre at \vec{x}_n is determined from the constrained path transform of the original image f , as discussed in Section 3.4.1. The length of the fibre at \vec{x}_n is taken to be the mode of the values of the opening transform at the cross-section of the fibre.

Having now determined fibre length and cross-sectional properties ξ_{ni} for a statistically significant number of random locations, we may construct the multivariate distributions of the measured quantities by statistical binning. As the probability to sample a fibre is proportional to its volume, the distributions will be of type

$$p(\xi_1, \xi_2, \dots, \xi_K) = \frac{1}{V} \frac{\partial^K V}{\partial \xi_1 \partial \xi_2 \dots \partial \xi_K}, \quad (3.32)$$

i.e., ξ_k -distributions of fibre phase volume V . The result may be transformed into the distribution of number of fibres by using Equation (3.30), but now the volume of a single fibre V_1 does not have to depend solely on its length and wall thickness. Instead, any of the quantities that appear in p may be arguments of V_1 , *e.g.*,

$$V_1(L, A) \propto LA, \quad (3.33)$$

where A is the measured cross-sectional area. Thus the assumption about geometrical similarity of fibres with respect to fibre wall thickness (Equation (3.31)) is significantly relaxed.

In [1] the method discussed above was tested on a specially fabricated material where hollow steel capillary tubes and solid copper wire served as fibres. The fibres were cut into predetermined lengths and mixed with molding rubber. The material was X- μ CT imaged with SkyScan 1172 device and the method discussed above was applied on it. Furthermore, the two types of fibres were separated from each other by considering the geometry of their cross-sections: simply connected cross-sections (*i.e.* those with no holes) were attributed to copper wire and others to capillary tube. Finally, aspect ratio distributions

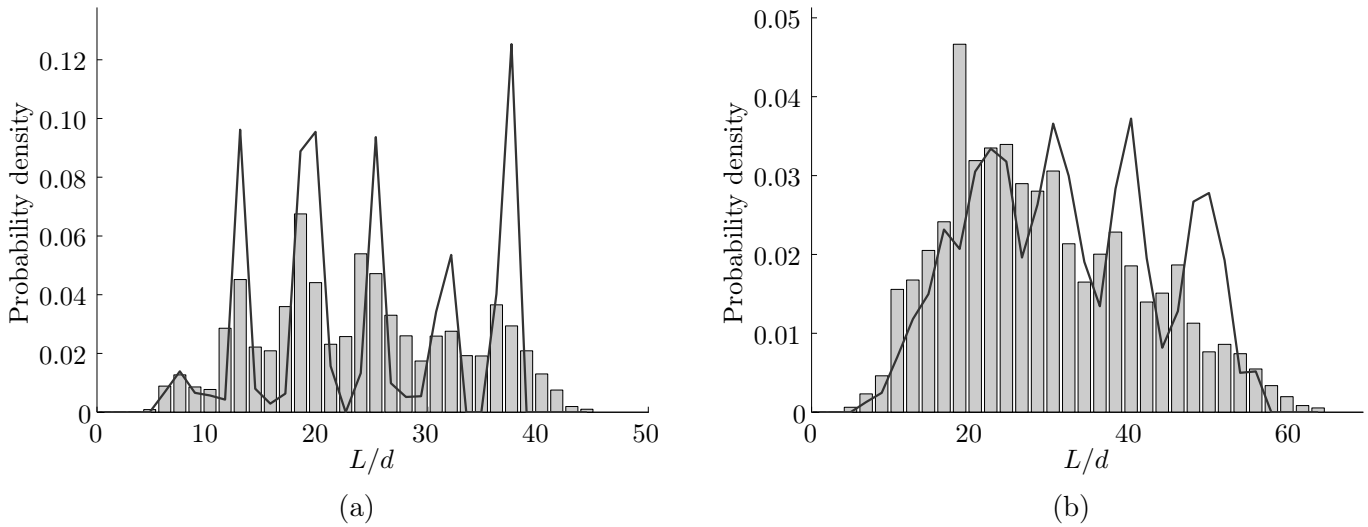


Figure 3.9: Aspect ratio distribution for (a) hollow fibres and (b) solid fibres in the model composite. The bar plot is the distribution as estimated by the X- μ CT method and the solid line is the reference distribution obtained from the independent manual counting method. [1]

for both types of fibres were constructed, see Figure 3.9.

To obtain a reference data set, the molding rubber was teared off and the two types of fibres were separated manually. The fibres were spread over a white background and photographed. The length of the fibres was measured manually from the images, facilitating determination of reference aspect ratio distributions.

The X- μ CT results and the reference distributions are plotted in Figure 3.9. Based on the results, the X- μ CT method seems to reproduce the peaks in the reference distribution at correct positions, but in a somewhat wider shape. The difference in the full width at half maximum between peak given by the X- μ CT method and the reference distribution is approximately 10% of the position of the respective peak.

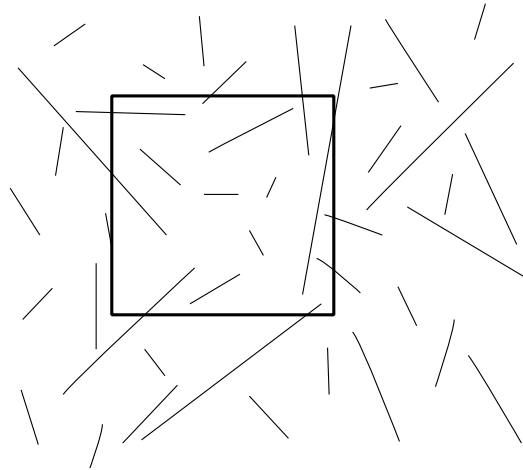


Figure 3.10: Sampling problem. Probability of a fibre (thin lines) to intersect with the sampling volume (rectangle) depends on the size of the fibre.

3.5 Finite size corrections

In Miettinen et al. [2] it was noted that the probability of a single particle to intersect the image volume depends on size, shape, orientation and spatial distribution of the particles. For example, in Figure 3.10 the longer lines intersect the edge of the sampling volume more often than the short ones do. If the length distribution of the lines is determined based on a finite sampling volume, the result is biased towards small line length.

In the field of stereology, special counting rules have been formulated to remove the bias [73]. The rules are based on omitting some of the particles during the measurement process. While analysing interconnected particles it is impossible to omit some of the particles as the individual particles have not been identified. Thus, other techniques are required in that case.

Based on results in Miettinen et al. [2] one can conclude that in the present context, the fibre length is the main quantity that may be affected by finite sampling volume, and thus we focus solely on that. To this end, we approximate the biased sampling process by a linear model

$$\bar{n} = \alpha n + \epsilon, \quad (3.34)$$

where $\bar{\mathbf{n}}$ is the biased fibre length distribution, \mathbf{n} is the non-biased fibre length distribution, $\boldsymbol{\alpha}$ is a measurement matrix describing the sampling process and $\boldsymbol{\epsilon}$ is an error vector. The problem of estimating \mathbf{n} is reduced into determining $\boldsymbol{\alpha}$ and inverting Equation (3.34).

It turns out that the components α_{ij} are proportional to the probability that a fibre whose length is l_j has a segment of length l_i in the sampling volume. Such a probability can be determined analytically for a given sampling volume [2], but it is much simpler to use a Monte Carlo simulation instead. To that end, a large space containing a sampling volume is first defined. The shape of the sampling volume must be similar to the shape of the tomographic image. A large number of lines of length l_j are deposited into the space and their length distribution in the sampling volume is determined. The length distribution, with proper binning and normalization, is the j :th column of $\boldsymbol{\alpha}$ [2]. Repeating the procedure for all j yields all columns of $\boldsymbol{\alpha}$.

Equation (3.34) cannot be solved for \mathbf{n} simply by inverting matrix $\boldsymbol{\alpha}$ because of the error vector $\boldsymbol{\epsilon}$. The problem is clearly ill-posed, whereby the generalized Tikhonov regularization is used instead [74] and the solution is written in the form

$$\mathbf{n} = \arg \min_{\mathbf{m}} (\|\boldsymbol{\alpha}\mathbf{m} - \bar{\mathbf{n}}\|^2 + \lambda \|\mathcal{L}\mathbf{m}\|^2), \quad (3.35)$$

where \mathcal{L} is a differencing operator

$$\mathcal{L}(\mathbf{m}) = (m_2 - m_1, m_3 - m_2, \dots). \quad (3.36)$$

In Figure 3.11 [2] the correction method discussed above has been applied to X- μ CT analysis of wood fibre composite material made of Kraft pulp fibres and polylactic acid (PLA) matrix. For reference, the fibre length distribution has been determined using an independent method based on dissolving the matrix in hot chloroform. As seen in the figure, the correction is rather minor, mostly because the mean fibre length (approximately 50 μm) is small compared to the diameter of the tomographic image (approximately 1 mm). Based on this and results shown in [2] it can be concluded as a rule-of-thumb

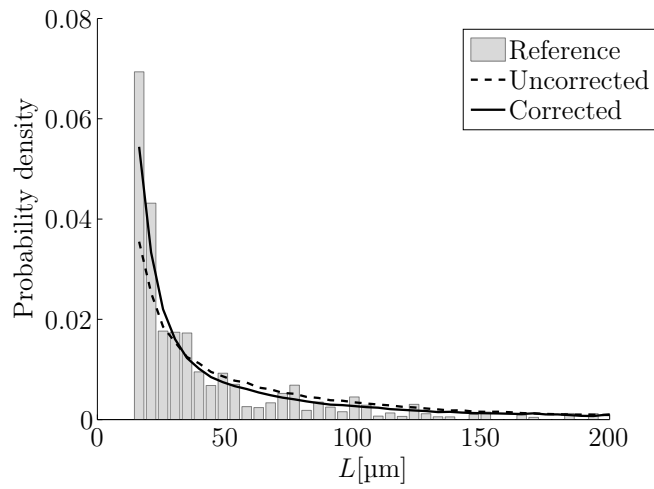


Figure 3.11: Correction for bias in fibre length caused by finite sampling volume for injection moulded Kraft pulp – polylactic acid composite material. [2]

that it is not necessary to perform the correction unless the uncorrected mean length is more than approximately 20% of image diameter.

Chapter 4

Applications

4.1 Micromechanical modelling

Within micromechanical modelling of composite materials, quantities related to the microscopic structure of the material are combined with the mechanical properties of the constituents, to arrive in estimates of mechanical properties of the composite material. Micromechanical models may be used, *e.g.*, to estimate the amount of reinforcement required for having given tensile properties in the final material.

In Miettinen et al. [1] and Miettinen et al. [7] we have demonstrated the use of X- μ CT analysis to estimate the parameters of a micromechanical model for the Young's modulus of flax fibre composites. The Young's moduli given by the model are compared to those from mechanical tests [75, 76].

Within the micromechanical model, the Young's modulus of the composite is estimated using a rule-of-mixtures equation [77]

$$E_c = (\eta_o \eta_l \phi_f E_f + \phi_m E_m)(1 - \phi_v)^2, \quad (4.1)$$

where E_c , E_m and E_f are Young's moduli of the composite, the matrix and the fibres, respectively; ϕ_f , ϕ_m and ϕ_v are the volume fractions of fibres,

matrix and void, respectively; and η_o and η_l are the orientation and the length efficiency factors, respectively [78, 79].

For determination of the orientation efficiency factor, the reinforcing fibres are divided into groups such that in each group all the fibres have the same orientation. The orientation efficiency factor η_o is then given by

$$\eta_o = \sum_n a_n \cos^4(\alpha_n), \quad (4.2)$$

where α_n is the angle between the loading direction and the direction of fibres in group n , and $a_n = \phi_{fn}/\phi_f$, where ϕ_{fn} is the volume fraction of fibres in group n .

The length efficiency factor is defined by

$$\eta_l = 1 - \frac{\tanh(L^*)}{L^*}, \quad (4.3)$$

where

$$L^* = 2 \frac{\langle L \rangle}{\langle d \rangle} \sqrt{\frac{G_m}{E_f \ln(\kappa/\phi_f)}} \quad (4.4)$$

and $\langle L \rangle$ is mean fibre length, $\langle d \rangle$ is mean fibre diameter, G_m is the shear modulus of matrix and κ is a geometrical packing pattern constant.

In the present case, the volume fractions of fibres, matrix and void for the test composites are determined using an independent gravimetric method. The shear modulus of matrix is determined from the Young's modulus by assuming isotropic material with Poisson's ratio 0.3. The Young's modulus of fibres is assumed to be $E_f = 50$ GPa [80]. Furthermore, the fibres are assumed to be packed hexagonally, implying $\kappa = \frac{\pi}{2\sqrt{3}} \approx 0.907$. The remaining parameters, $\langle L \rangle$, $\langle d \rangle$ and η_o are determined using the X- μ CT method of Section 3.4.2 and, for comparison, an independent reference method.

The independent reference method is based on dissolving the matrix in hot chloroform and determining the lengths of the remaining fibres manually with help of a microscope [81]. Small particles of fibre wall, *i.e.* fines, are

discarded from the analysis by visual inspection. The orientation efficiency factor is hard to determine using the reference method, so we have fitted the results of Equation (4.1) into the results of mechanical tests using η_o as a free parameter.

In the X- μ CT method visual inspection cannot be used to discard fines, but an algorithm must be used instead. Therefore we identify L^* as a dimensionless fibre length parameter and calculate its value for each fibre cross-section, replacing average length and diameter with those of the cross-section. A natural cut-off is obtained by excluding cross-sections with $L^* < 1$ from the calculation of η_o and η_l .

The Young's modulus given by Equation (4.1) is shown in Figure 4.1 for parameters determined using the X- μ CT method and the reference method. The results from mechanical tests are also shown. The correspondence between the Young's moduli estimated using the different methodologies is very good. However, the volume fraction of fibres discarded as fines is high (near 50%), highlighting the need to develop micromechanical models that can tolerate the presence of fines in addition to intact reinforcing fibres. If such a model was available, the X- μ CT method could likely be used to estimate all of its parameters.

4.2 Morphological degradation of fibres in injection moulding process

In an injection moulding process, the reinforcing fibres are subjected to large temperature and stress. If the fibres are fragile they may disintegrate longitudinally or transversally and thus their aspect ratio may change. As the length and the aspect ratio of fibres are important parameters affecting the mechanical properties of the composite material (see also Section 4.1), quantification of their changes during processing is of interest.

The reinforcing fibres in different processing stages of wood fibre – polylactic

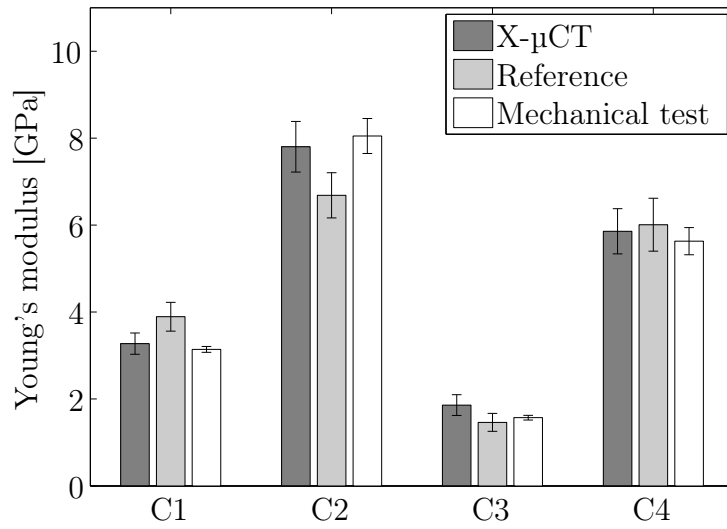


Figure 4.1: Estimates of Young's modulus of flax fibre – polylactic acid composites.

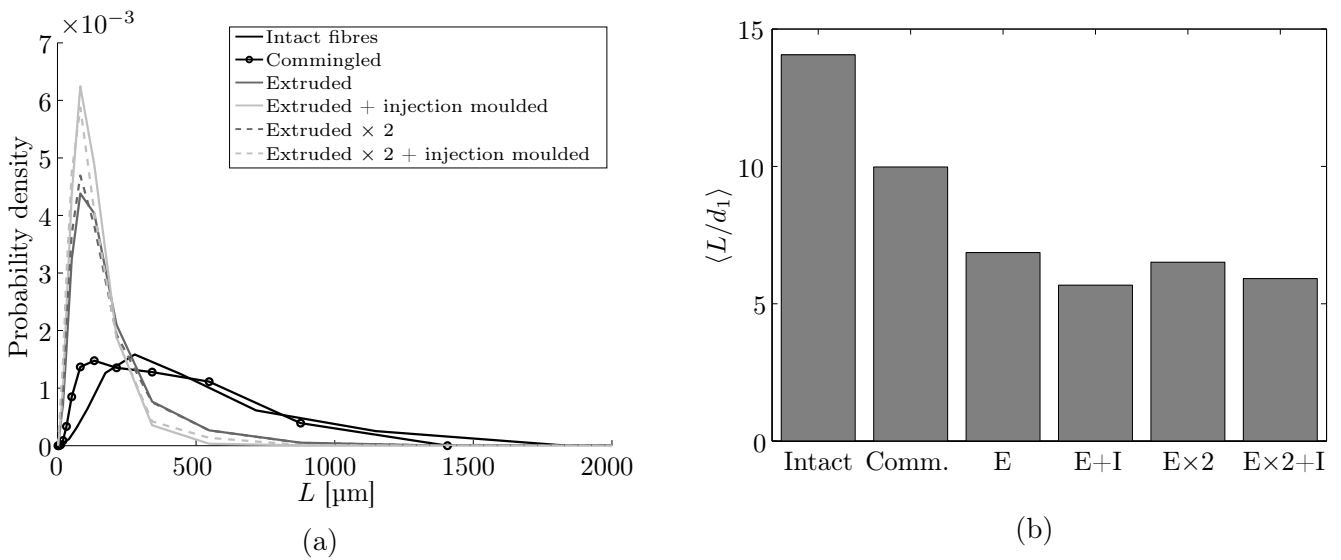


Figure 4.2: (a) Fibre length distribution and (b) average aspect ratio in different processing phases. 'Intact', 'Comm.', 'E', and 'I' stand for intact fibres, commingled fibres, extrusion and injection moulding, respectively. [3, 8].

acid (PLA) composite were studied in Joffre et al. [3] and in Gamstedt et al. [8]. Bleached sulphite wood fibres were first commingled with fibrous PLA. To reduce porosity, the mix was extruded once or twice and chopped into pellets to ease processing. The wood fibre – PLA pellets were then injection moulded into tensile test specimens. Samples for X- μ CT analysis were taken after each processing phase.

X- μ CT images of the samples were taken with XRadia microCT-400 device. The images were binarized and the length and the cross-sectional area of fibres was determined as described in Section 3.4.2. In the case of commingled fibre mat containing both wood fibres and fibrous PLA, cross-sectional samples of the two phases had to be separated. Therefore the convex area A_C of each fibre cross-section was also determined. All the cross-sectional samples not satisfying

$$A_C - A > 0.1A, \quad (4.5)$$

where A is the area of the fibre cross-section, were classified as PLA fibres and were not included in the results shown in Figure 4.2. An example of cross-sectional slices of a wood fibre and a PLA fibre are shown in Figure 4.3.

The resulting length distributions in Figure 4.2(a) show that the fibre length is retained in the commingling process. The most significant fibre length reduction occurs in the the extrusion step. However, the twice extruded sample does not show any further reduction in fibre length compared to the sample extruded once. The insignificant difference between once and twice extruded samples suggests that the fibres could stay longer without compromising quality of the pellets if the extrusion was performed multiple times but in gentler processing conditions. Anyway, in the present manufacturing process, efforts to retain fibre length should be placed on the extrusion step.

The average aspect ratio of fibres in Figure 4.2(b) shows somewhat different trend. The aspect ratio decreases already in the commingling process, but in the injection moulding the aspect ratio stays approximately constant. This hints that in the injection moulding process the fibres are disintegrated approximately equally both in the longitudinal and in the transverse directions.

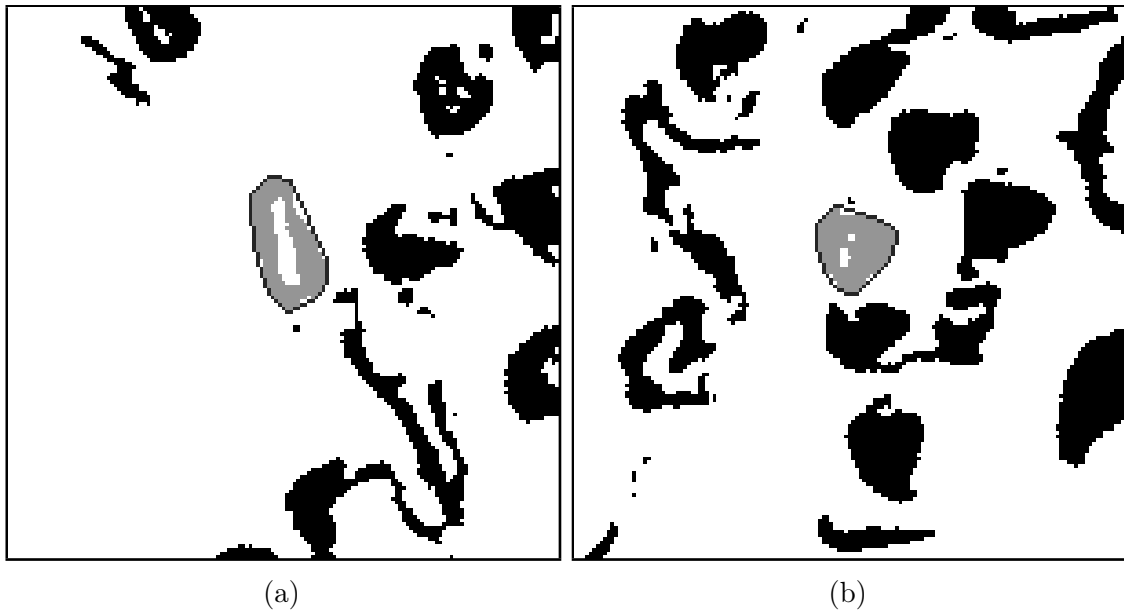


Figure 4.3: Cross-sectional slice of (a) wood fibre and (b) PLA fibre in commingled wood fibre – PLA fibre mat. The cross-section has been colored gray. The black parts are cross-sections of neighbouring fibres. The dark border around the gray part shows the edges of the convex hull of the cross-section.

Based on the results, X- μ CT techniques seem to be applicable in quantification of microstructural parameters of materials for the purpose of optimization of processing conditions. It is particularly important to notice that the material could be assessed with the same algorithm in all the processing phases, ensuring comparability of the results. The possibility to quantify the effect of various manufacturing processes on the microstructure of the material could assist in developing novel processes that do not degrade fibres as much as traditional methods.

4.3 Swelling of fibres

Although cellulose fibres are an inexpensive, light and biodegradable alternative to synthetic fibres, one of the primary drawbacks in using them is their ability to absorb water from the environment. Water intake leads to dimensional instability and weakening of composite structures.

In Joffre et al. [4] X-ray microtomography was shown to be a practical tool in assessing the moisture sensitivity of wood fibres and composite structures. X- μ CT images were taken from samples of free fibres and fibres embedded in matrix, both in dry (regulated room humidity, approximately 35% relative humidity) and in wet (nominal 100% relative humidity) atmosphere. An operator marked perimeter of 30 fibres from each X- μ CT image. The identified perimeters were used to determine the swelling coefficient of the fibres. Finally, a finite element model of fibre swelling was constructed and validated using the measured swelling coefficients.

It is of interest to notice that the fibres exhibit many sizes and cross-sectional shapes. In addition, in the manual method the amount of samples taken from each image is relatively small and thus statistics of fibre shapes is limited. It is thus advantageous to sample the same locations both in dry and in wet state. To facilitate such sampling, the X- μ CT images were taken from the same sample in both states by applying a special sample holder (Figure 4.4(a)).

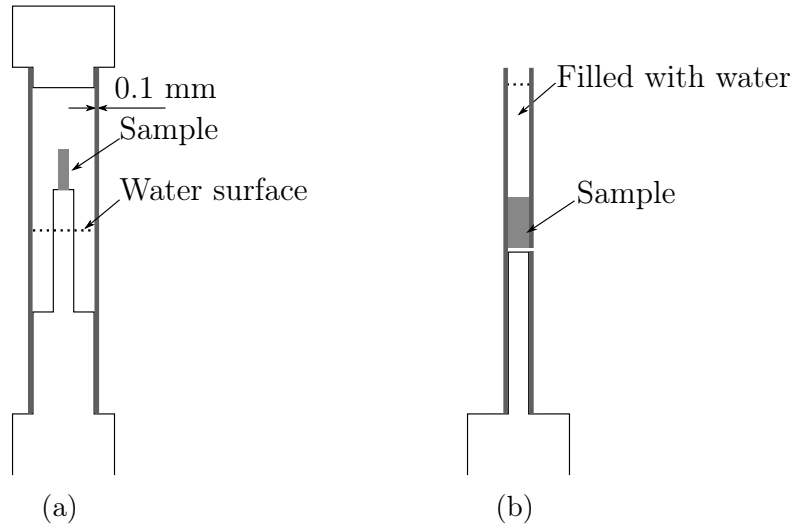


Figure 4.4: (a) Schematics of a sample holder used to scan samples in regulated 35 % relative humidity and in nominal 100 % relative humidity. (b) Schematics of a sample holder that could be used to study imbibition of water into a sample from single direction.

The sample holder is constructed such that the sample can be enclosed in an air-tight chamber during the X- μ CT scan. The sample is first imaged in a dry state and the top cap of the sample chamber is open. Thus, the sample is in the room humidity. After the first scan, a drop of water is added to the bottom of the sample chamber and the top cap is installed, causing the relative humidity inside the chamber to increase to nominal 100 %. After the sample has stabilized into the changed environment, it is imaged again. Two images of the very same sample in wet and dry state are thus obtained.

To reduce X-ray attenuation into the chamber, its walls are made of light material as thin as possible. In Joffre et al. [4] 0.1 mm thick poly(methyl methacrylate) tube (*i.e.* PMMA drinking straw) was used, but later it was found out that polyether ether ketone (PEEK) has favorable machining properties, enabling manufacturing of more complex systems. For example, in Miettinen et al. [82] a sample holder made of PEEK tube was demonstrated, with wall thickness 0.1 mm and tube ends connected to threaded fittings. The sample chambers discussed here cause approximately 10 % decrease in X-ray intensity, thereby increasing image acquisition time only a little.

The sample holder applied in Joffre et al. [4] could be easily modified for other kind of wetting processes, too. For example, a one-dimensional imbibition process could be realized with sample and holder geometry shown in Figure 4.4(b), where liquid water touches the sample only at a single face. Such extensions are left as topics for future work, together with related algorithms for determination of, *e.g.*, local water concentration.

Chapter 5

Summary

Measurement methods for estimating microstructural properties of short fibre composite materials were developed. The methods are based on analysing X-ray microtomographic images of composite material samples. In particular, the focus was on methods to determine the length and the cross-sectional property distributions of fibres. The developed methods were validated using experimental data and applied in estimating properties of natural fibre composites.

The experimental validation of the algorithms was performed using a model composite made of metallic fibres and rubber. The aspect ratio distribution in the model composite was estimated both manually and using the developed methods. Comparison of the results showed good correspondence between the two methodologies.

The effect of finite size of the image volume was discussed. It was concluded that the fibre length distribution is the quantity that is most affected by the finite volume. A method to correct the bias caused by finite volume effects was introduced. Finally it was noted that the correction is virtually unnecessary for the short-fibre composites analysed in the rest of the thesis.

It was shown that the developed algorithms can be used to successfully estimate the parameters of a particular micromechanical model. Modelling re-

sults were compared to those from mechanical tests, showing good agreement. It was noted that many rule-of-mixtures-based micromechanical models disregard fines, *i.e.*, particulate material smaller than reinforcing fibres. Such fines often occur in natural fibre composites, partially caused by naturally wide size distribution of the fibres and partially by disintegration of fibres in the manufacturing process. In manual measurements fines are often discarded by visual inspection. On the other hand, X- μ CT images contain information on all particles discernible within the limits set by resolution and sample size, typically including a large part of fines. Such information could support the design of more advanced models that account for the presence of a fine particulate material phase.

The image processing algorithms were also applied in studying the degradation of wood fibres in an injection moulding process. Significant decrease was observed in fibre length and aspect ratio, occurring mostly in the extrusion phase. As both quantities affect mechanical properties of the composite, it was concluded that gentler manufacturing processes would be desirable for this type of composite material.

Finally, the non-destructive nature of X- μ CT was applied in studying the hygroexpansion of fibres in wood fibre – polylactic acid composite materials. The same material sample was imaged twice, first in room humidity and then in nominal 100 % relative humidity. Correlation between the images was used to find the same wood fibres in dry and wet states. The geometrical properties of the fibres were determined manually and used to calculate swelling coefficient of the fibres. Finally, results on the swelling coefficient were used to validate a finite element model.

Based on results discussed in this thesis, methods relying on X- μ CT imaging seem to be well suited for analysis of natural fibre composites. In particular, X- μ CT methods allow assessing the material with high precision. Such a possibility may assist in achieving future advances both in manufacturing and in modelling of composite materials.

Bibliography

- [1] A. Miettinen, A. Ojala, L. Wikström, R. Joffe, B. Madsen, K. Nättinen, and M. Kataja. Non-destructive automatic determination of aspect ratio and cross-sectional properties of fibres. *Composites: Part A*, 77: 188–194, 2015.
- [2] A. Miettinen, C. L. Luengo Hendriks, G. Chinga-Carrasco, E. K. Gamstedt, and M. Kataja. A non-destructive X-ray microtomography approach for measuring fibre length in short-fibre composites. *Composites Science and Technology*, 72(15):1901–1908, October 2012.
- [3] T. Joffe, A. Miettinen, F. Berthold, and E. K. Gamstedt. X-ray micro-computed tomography investigation of fibre length degradation during the processing steps of short-fibre composites. *Composites Science and Technology*, 105:127–133, 2014.
- [4] T. Joffe, E. Wernersson, A. Miettinen, C. L. Luengo Hendriks, and E. K. Gamstedt. Swelling of cellulose fibres in composite materials: Constraint effects of the surrounding matrix. *Composites Science and Technology*, 74:52–59, 2013.
- [5] T. Joffe, A. Miettinen, E. Wernersson, P. Isaksson, and E. K. Gamstedt. Effects of defects on the tensile strength of heterogeneous composite materials. *Mechanics of materials*, 75, 2014.
- [6] A. Miettinen and K. Kataja. Non-destructive analysis of fiber properties using 3D X-ray microtomographic data. In S. Fæster, D. Juul Jensen, B. Ralph, and B.F. Sørensen, editors, *Proceedings of the 32nd Risø*

International Symposium on Materials Science: Composite materials for structural performance – towards higher limits. Risø National Laboratory for Sustainable Energy, Technical University of Denmark, 2011. ISBN 978-87-550-3925-4.

- [7] A. Miettinen, R. Joffe, B. Madsen, K. Nättinen, and K. Kataja. Quantitative analysis of length-diameter distribution and cross-sectional properties of fibers from three-dimensional tomographic images. In B. Madsen, H. Lilholt, Y. Kusano, S. Fæster, and B. Ralph, editors, *Proceedings of the 34th Risø International Symposium on Materials Science: Processing of fibre composites – challenges for maximum materials performance*. Department of Wind Energy, Risø Campus, Technical University of Denmark, 2013.
- [8] E. K. Gamstedt, T. Joffe, A. Miettinen, and F. Berthold. Monitoring of fibre length degradation during processing of short-fibre composites by use of X-ray computed tomography. In B. Madsen, H. Lilholt, Y. Kusano, S. Fæster, and B. Ralph, editors, *Proceedings of the 34th Risø International Symposium on Materials Science: Processing of fibre composites – challenges for maximum materials performance*. Department of Wind Energy, Risø Campus, Technical University of Denmark, 2013.
- [9] A. Miettinen, R. Joffe, L. Pupure, and B. Madsen. Identification of true microstructure of composites based on various flax fibre assemblies by means of three-dimensional tomography. In *Proceedings of the 20th International Conference on Composite Materials*. International Committee on Composite Materials, 2015.
- [10] A. Miettinen, A. Ekman, G. Chinga-Carrasco, and M. Kataja. On the intrinsic thickness of nanocellulose films. *Journal of Materials Science*, 50(21):6926–6934.
- [11] S.V. Joshia, L.T. Drzalb, A.K. Mohanty, and S. Arora. Are natural fiber composites environmentally superior to glass fiber reinforced composites? *Composites Part A*, 35:371–376, 2004.

- [12] C.-F. Yang, A.R.K. Eusufzai, R. Sankar, R.E. Mark, and R.W. Jr. Perkins. Measurements of geometrical parameters of fiber networks. Part 1. *Svensk Papperstidning*, 81(13):426–433, 1978.
- [13] D. Gelber. Thin sectioning: Details of techniques. *The Journal of Biophysical and Biochemical Cytology*, 3(2), 1957.
- [14] O. W. Richards. *The effective use and proper care of the microtome*. American Optical Company, 1959.
- [15] M. Aronsson, O. Henningsson, and Ö. Sävborg. Slice-based digital volume assembly of a small paper sample. *Nordic Pulp and Paper Research Journal*, 17(1), 2002.
- [16] W. Denk and H. Horstmann. Serial block-face scanning electron microscopy to reconstruct three-dimensional tissue nanostructure. *PLoS Biology*, 2(11), 10 2004.
- [17] G. Chinga, P. O. Johnsen, and O. Diserud. Controlled serial grinding for high-resolution three-dimensional reconstruction. *Journal of Microscopy*, 214(1):13–21, 2004.
- [18] S. Torquato. *Random Heterogeneous Materials*. Springer, 2002.
- [19] T. Hildebrand and P. Rüeeggsegger. A new method for the model-independent assessment of thickness in three-dimensional images. *Journal of Microscopy*, 185(1):67–75, 1997.
- [20] J. Serra. *Image analysis and mathematical morphology*. Academic Press, 1982. ISBN 0-12-637240-3.
- [21] B. Jähne. *Practical handbook on image processing for scientific and technical applications*. CRC Press, 2004.
- [22] A. Clarke and C. Eberhardt. The representation of reinforcing fibres in composites as 3D space curves. *Composites Science and Technology*, 59(8):1227–1237, 1999.

- [23] H. Yang and W. B. Lindquist. Three-dimensional image analysis of fibrous materials. In *Proceedings of SPIE*, volume 4115, pages 275–282, 2000.
- [24] C. N. Eberhardt and A. R. Clarke. Automated reconstruction of curvilinear fibres from 3D datasets acquired by X-ray microtomography. *Journal of Microscopy*, 206(1):41–53, 2002.
- [25] J. C. Tan, J. A. Elliott, and T. W. Clyne. Analysis of tomography images of bonded fibre networks to measure distributions of fibre segment length and fibre orientation. *Advanced Engineering Materials*, 8(6):495–500, 2006.
- [26] T. Walther, K. Terzic, T. Donath, H. Meine, F. Beckmann, and H. Thoenen. Microstructural analysis of lignocellulosic fiber networks. In *Proceedings of SPIE*, volume 6318, pages 631812–631812–10, 2006.
- [27] M. Axelsson. 3D tracking of cellulose fibres in volume images. In *IEEE International Conference on Image Processing, 2007*, volume 4, pages IV–309–IV–312, 2007.
- [28] E. L. G. Wernersson, A. Brun, and C. L. Luengo Hendriks. Segmentation of wood fibres in 3D CT images using graph cuts. In P. Foggia, C. Sansone, and M. Vento, editors, *Image Analysis and Processing – ICIAP 2009*, volume 5716 of *Lecture Notes in Computer Science*, pages 92–102. Springer Berlin Heidelberg, 2009.
- [29] S. Kärkkäinen, J. Nyblom, A. Miettinen, T. Turpeinen, and P. Pötschke. Stochastic shape model for fibres with an application to carbon nanotubes. In V. Capasso et al., editor, *Proceedings of the 10th European Congress of ISS*, Bologna, Italy, 2009. ESCULAPIO Pub. Co. The MIRIAM Project Series.
- [30] M. Teßmann, S. Mohr, S. Gayetsky, U. Haßler, R. Hanke, and G. Greiner. Automatic determination of fiber-length distribution in composite material using 3D CT data. *EURASIP Journal of Advanced Signal Processing*, 2010, 2010.

- [31] J. Lux, C. Delisée, and X. Thibault. 3D characterization of wood based fibrous materials: an application. *Image Analysis & Stereology*, 25(1), 2011.
- [32] F. Malmberg, J. Lindblad, C. Östlund, K. M. Almgren, and E. K. Gamstedt. Measurement of fibre-fibre contact in three-dimensional images of fibrous materials obtained from X-ray synchrotron microtomography. *Nuclear Instruments and Methods in Physics Research Section A: Accelerators, Spectrometers, Detectors and Associated Equipment*, 637(1): 143–148, 2011.
- [33] D. Tsarouchas and A. E. Markaki. Extraction of fibre network architecture by X-ray tomography and prediction of elastic properties using an affine analytical model. *Acta Materialia*, 59(18):6989–7002, 2011.
- [34] S. Kärkkäinen, A. Miettinen, T. Turpeinen, J. Nyblom, J. Timonen, and P. Pötschke. A stochastic shape and orientation model for planar fibres with an application to carbon nanotubes. *Image Analysis & Stereology*, 31(1):17–26, 2012.
- [35] J. Viguié, P. Latil, L. Orgéas, P. J. J. Dumont, S. Rolland du Roscoat, J.-F. Bloch, C. Marulier, and O. Guiraud. Finding fibres and their contacts within 3D images of disordered fibrous media. *Composites Science and Technology*, 89:202–210, 2013.
- [36] J. Radon. Über die bestimmung von funktionen durch ihre integralwerte längs gewisser mannigfaltigkeiten. *Berichte der Sächsischen Akademie der Wissenschaft*, 69:262–277, 1917. Translated to English by P. C. Parks to appear in On the determination of functions from their integral values along certain manifolds, *IEEE Transactions on Medical Imaging*, 5(4), 170-176, 1986.
- [37] M. S. Kaczmarz. Angenäherte auflösung von systemen linearer gleichungen. *Bulletin International de l'Académie Polonaise des Sciences et des Lettres A*, 37(355–357), 1937. Translated to English by J. P.

- Stockmann, to appear in PhD thesis *New strategies for accelerated spatial encoding with quadratic fields in magnetic resonance imaging*, 2012, Yale University, New Haven, Connecticut, USA.
- [38] R. N. Bracewell and A. C. Riddle. Inversion of fan-beam scans in radio astronomy. *Astrophysical Journal*, 150:427–434, 1967.
- [39] Z. V. Maizlin and P. M. Vos. Do we really need to thank the beatles for the financing of the development of the computed tomography scanner? *Journal of Computer Assisted Tomography*, 36(2):161–164, 2012.
- [40] G. N. Ramachandran and A. V. Lakshminarayanan. Three-dimensional reconstruction from radiographs and electron micrographs: Application of convolutions instead of fourier transforms. *Proceedings of the National Academy of Sciences of the United States of America*, 68(9):2236–2240, 1971.
- [41] L. A. Shepp and B. F. Logan. The fourier reconstruction of a head section. *Nuclear Science, IEEE Transactions on*, 21(3):21–43, 1974.
- [42] Nobel Media. The nobel prize in physiology or medicine 1979. http://www.nobelprize.org/nobel_prizes/medicine/laureates/1979/, 1979. Accessed 28 Aug 2014.
- [43] J. C. Elliott and S. D. Dover. X-ray microtomography. *Journal of Microscopy*, 126(2):211–213, 1982. ISSN 1365-2818.
- [44] L. A. Feldkamp, L. C. Davis, and J. W. Kress. Practical cone-beam algorithm. *Journal of Optical Society of America A*, 1(6), 1984.
- [45] A. C. Kak and M. Slaney. *Principles of computerized tomographic imaging*. IEEE Press, 1988.
- [46] A. C. Thompson, editor. *X-ray data booklet*. Center for X-ray optics, Advanced Light Source, Lawrence Berkeley National Laboratory, University of California, Berkeley, California, USA, 3 edition, 2009.
- [47] Hamamatsu Photonics KK. *Marketing material*, 2014.

- [48] Excillum AB. *Marketing material*, 2014.
- [49] S. R. Stock. *Microcomputed tomography*. CRC Press, 2009.
- [50] W. van Aarle. *Tomographic segmentation and discrete tomography for quantitative analysis of transmission tomography data*. PhD thesis, Vision Lab, Department of Physics, University of Antwerp, 2012.
- [51] R. C. Gonzalez and R. E. Woods. *Digital Image Processing*. Prentice-Hall, 2 edition, 2002.
- [52] T. Turpeinen. *Analysis of microtomographic images of porous heterogeneous materials*. PhD thesis, Jyväskylä, Finland, 2015.
- [53] S. M. Smith and J. M. Brady. SUSAN – a new approach to low level image processing. *International Journal of Computer Vision*, 23(1): 45–78, 1997.
- [54] P. Perona and J. Malik. Scale-space and edge detection using anisotropic diffusion. *IEEE Transactions on Pattern Analysis and Machine Intelligence*, 12(7):629–639, 1990.
- [55] A. Buades, B. Coll, and J.-M. Morel. A non-local algorithm for image denoising. In *Proceedings of the IEEE Computer Society Conference on Computer Vision and Pattern Recognition*, volume 2, pages 60–65. IEEE, 2005.
- [56] Metso Automation OY. *Marketing material*, 2014.
- [57] P. A. Reme and T. Helle. Assessment of transverse dimensions of wood tracheids using SEM and image analysis. *Journal of Pulp and Paper Science*, 28(4), 2001.
- [58] R. Joffe, B. Madsen, K. Nättinen, and A. Miettinen. Strength of cellulosic fiber/starch acetate composites with variable fiber and plasticizer content. *Journal of Composite Materials*, 49(8):1007–1017, 2014.

- [59] V. Koivu, M. Decain, C. Geindreau, K. Mattila, J. Alaraudanjoki, J.-F. Bloch, and M. Kataja. Flow permeability of fibrous porous materials. Micro-tomography and numerical simulations. In S. I’Anson, editor, *Proceedings of the 14th Fundamental Research Symposium*, pages 437–454. The Pulp and Paper Fundamental Research Society, 2009.
- [60] V. Koivu, M. Decain, C. Geindreau, K. Mattila, J.-F. Bloch, and M. Kataja. Transport properties of heterogeneous materials. Combining computerised X-ray micro-tomography and direct numerical simulations. *International Journal of Computational Fluid Dynamics*, 23(10):713–721, 2009.
- [61] A. Rosenfeld and J. L. Pfaltz. Sequential operations in digital picture processing. *Journal of the association for computing machinery*, 13(4):471–494, 1966.
- [62] W. E. Lorensen and H. E. Cline. Marching cubes: A high resolution 3D surface construction algorithm. In *Proceedings of the 14th Annual Conference on Computer Graphics and Interactive Techniques*, SIGGRAPH 1987, pages 163–169, New York, NY, USA, 1987. ACM.
- [63] J. Lindblad and I. Nyström. Surface area estimation of digitized 3D objects using local computations. In *Proceedings of the 10th International Conference on the Discrete Geometry for Computer Imagery*, pages 267–278, Bordeaux, France, 2002. Springer.
- [64] R. Klette and H. Sun. Digital planar segment based polyhedrization for surface area estimation. In C. Arcelli, L. P. Cordella, and G. Sanniti di Baja, editors, *Visual Form 2001*, volume 2059 of *Lecture Notes in Computer Science*, pages 356–366. Springer Berlin Heidelberg, 2001.
- [65] D. Coeurjolly, F. Flin, O. Teytaud, and L. Tougne. Multigrid convergence and surface area estimation. In T. Asano, R. Klette, and C. Ronse, editors, *Geometry, Morphology, and Computational Imaging*, volume 2616 of *Lecture Notes in Computer Science*, pages 101–119. Springer Berlin Heidelberg, 2003.

- [66] K. Pearson. On lines and planes of closest fit to systems of points in space. *Philosophical Magazine*, 2:559–572, 1901.
- [67] R. A. Jarvis. On the identification of the convex hull of a finite set of points in the plane. *Information Processing Letters*, 2:18–21, 1973.
- [68] C. L. Luengo Hendriks and L. J. van Vliet. A rotation-invariant morphology for shape analysis of anisotropic objects and structures. In C. Arcelli, L. P. Cordella, and G. Sanniti di Baja, editors, *Proceedings of the 4th International Workshop on Visual Form*, pages 378–387. Springer-Verlag Berlin Heidelberg, 2001.
- [69] G. Matheron. *Random sets and integral geometry*. John Wiley and Sons, New York, 1975.
- [70] C. L. Luengo Hendriks. Constrained and dimensionality-independent path openings. *IEEE Transactions on Image Processing*, 19(6):1587–1595, 2010.
- [71] H. Heijmans, M. Buckley, and H. Talbot. Path openings and closings. *Journal of Mathematical Imaging and Vision*, 22(2-3):107–119, 2005.
- [72] H. Talbot and B. Appleton. Efficient complete and incomplete path openings and closings. *Image and Vision Computing*, 25(4):416–425, 2007. International Symposium on Mathematical Morphology 2005.
- [73] P. R. Mouton. *Principles and Practices of Unbiased Stereology: An Introduction for Bioscientists*. Johns Hopkins University Press, Baltimore, MD, USA, 2002.
- [74] A. N. Tikhonov and V. Y. Arsenin. *Solutions of ill-posed problems*. Winston & Sons, 1977.
- [75] B. Madsen, R. Joffe, H. Peltola, and K. Nättinen. Short cellulosic fiber/starch acetate composites – micromechanical modeling of Young’s modulus. *Journal of Composite Materials*, 45(20):2119–2131, 2011.

- [76] K. Nättinen, S. Hyvärinen, R. Joffe, L. Wallström, and B. Madsen. Naturally compatible: Starch acetate/cellulosic fiber composites. I. Processing and properties. *Polymer Composites*, 31(3):524–535, 2010.
- [77] B. Madsen, A. Thygesen, and H. Lilholt. Plant fibre composites – porosity and stiffness. *Composites Science and Technology*, 69(7–8): 1057–1069, 2009.
- [78] H. Krenchel. *Fibre reinforcement*. PhD thesis, Copenhagen, Denmark, 1964.
- [79] H. L. Cox. The elasticity and strength of paper and other fibrous materials. *British Journal of Applied Physics*, 3:72–79, 1952.
- [80] H. Lilholt and J. M. Lawther. Natural organic fibres. In A. Kelly and C. Zweben, editors, *Comprehensive composite materials*, volume 1, chapter 10, pages 303–325. Elsevier Science, Amsterdam, 2000.
- [81] H. Peltola, B. Madsen, R. Joffe, and K. Nättinen. Experimental study of fiber length and orientation in injection molded natural fiber/starch acetate composites. *Advances in materials science and engineering*, 2011.
- [82] A. Miettinen, G. Chinga-Carrasco, and M. Kataja. Three-dimensional microstructural properties of nanofibrillated cellulose films. *International Journal of Molecular Sciences*, 15(4):6423–6440, 2014.